# Multimodal antireflective coatings for perfecting anomalous reflection from arbitrary periodic structures

Sherman W. Marcus [ORCID],[*] Vinay K. Killamsetty [ORCID], Yarden Yashno [ORCID], and Ariel Epstein [ORCID]

*Andrew and Erna Viterbi Faculty of Electrical and Computer Engineering, Technion-Israel Institute of Technology, Haifa 3200003, Israel*

Metasurfaces and metagratings possess vast wave-manipulation capabilities, including reflection and refraction of a plane wave into nonstandard directions. These require meticulously-designed subwavelength meta-atoms in each period of the metasurface which guarantee unitary coupling to the desired Floquet-Bloch mode or, equivalently, suppression of the coupling to other modes. Herein, we propose an entirely different scheme to achieve such modal control. Extending the concept of antireflective coatings to enable simultaneous manipulation of multiple modes, we show theoretically and experimentally that a simple superstrate consisting of only several uniform dielectric layers can be modularly applied to *arbitrary* periodic structures to yield perfect anomalous reflection. This multimodal antireflective coating (MMARC), designed based on an analytical model, presents a conceptually and practically simpler paradigm for wave control across a wide range of physical branches, from electromagnetics and acoustics to seismics and beyond.

## I. INTRODUCTION

Metasurfaces have been shown to possess wave control capabilities not previously available, both for transmission through them and for reflection from them [1–3]. These typically-periodic structures consist of discrete subwavelength cells (meta-atoms) which are meticulously designed to provide the desired scattered fields. A higher density of meta-atoms typically provides fields closer to the design goals at the expense of increased design and fabrication complexity. The wave control capabilities are often demonstrated by designs, which reflect [4,5] or transmit [6–12] an incident plane wave into a single nonstandard direction (anomalous reflection or refraction), or into multiple nonstandard directions (beam-splitting) [13].

Huygens' metasurfaces (HMSs) [10–12] successfully produced anomalous refraction for moderate refraction angles, but at extreme angles wave-impedance mismatch led to the additional presence of a specularly reflected wave [12,14]. This failure was overcome by omega bianisotropic metasurfaces (OBMSs), which introduced an additional magnetoelectric degree of freedom, leading to a metasurface capable of producing *perfect* anomalous reflection, refraction and beam splitting [13,15–17]; perfect in the sense that all incident power is transferred to the desired anomalously scattered wave(s). Comparing analytical solutions for both the HMS [18] and the OBMS [19], we recently employed a ray-optics interpretation of the process to demonstrate the equivalence between an OBMS, and a HMS with a virtual antireflective coating (ARC) [19,20]. The purpose of the ARC (be it virtual [19] or real [21–24]) is, of course, to utilize a planar dielectric surface to suppress a

*single*, unwanted specularly reflected mode, which is done by ensuring the resulting multiply-reflected waves add up destructively.

In contrast to metasurfaces which generally require dense meta-atoms, metagratings are characterized by sparse meta-atoms consisting of individual scatterers distributed periodically over a surface [25]. By accounting for the interactions of these scatterers with each other and with an incidence field, their parameters are designed to produce desired Floquet-Bloch wave amplitudes with very high efficiency [25–35]. Although metagratings provide an excellent alternative to metasurfaces with densely packed meta-atoms, it should be kept in mind that engineering of the periodic structure is still necessary, and this might be challenging at certain operating regimes and for certain physical systems [27,36]. In addition, in many instances, a simplified design approach and/or manufacturing inaccuracies can lead to fabricated devices that are periodic, but exhibit suboptimal performance.

In this paper, we suggest and demonstrate experimentally that the ARC principle of utilizing a planar surface to suppress a single mode can be broadened to suppressing *multiple* modes (Fig. 1). That is, the task of modal suppression that for metagratings was performed by a periodic array of individual scatters, can be performed by a simple dielectric stack which we refer to as a *multimodal* antireflective coating (MMARC). Since the dielectric layers of the MMARC are uniform, the Floquet-Bloch modes must be produced by a separate periodic surface to which the MMARC is affixed (Fig. 1). We will refer to this separate surface as a "basic periodic surface" (BPS). The only requirement on the BPS is that it be periodic with the desired period, so that it can produce Floquet-Bloch waves in the desired directions. Once the BPS is given, it is not tampered with; the design applies only to the MMARC layers which are adjusted to produce the desired Floquet-Bloch amplitudes of the scattered wave, a
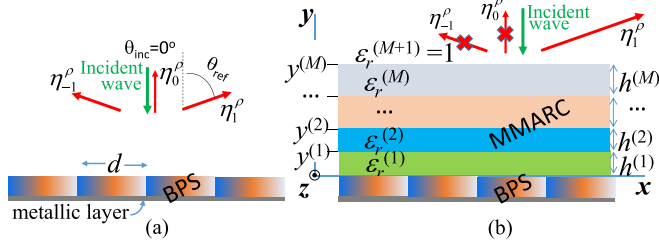
─────────
*shermanm@technion.ac.il

FIG. 1. A $d$-periodic, impenetrable, simple basic periodic surface (BPS) for reflecting a normally incident wave into directions $\pm\theta_{\mathrm{ref}}$ and $0°$. (a) Without the MMARC, the amplitudes of these FB reflected waves are finite. (b) With a properly designed MMARC, all but the desired FB wave are suppressed. The MMARC consists of $M$ uniform dielectric layers; the thickness of layer $m$ is $h^{(m)}$, its upper surface is at $y = y^{(m)}$, and its relative permittivity is $\epsilon_r^{(m)}$. $\eta_p^\rho$ is the relative power coupled to reflected mode $p$.

paradigm which can open up a myriad of novel wave-control possibilities.

This BPS-MMARC approach introduces several appealing features. First, a MMARC can be designed for *any arbitrary* BPS, including surfaces that have not undergone specialized design procedures; in fact, they can take many forms (in terms of geometry and material composition), be irregular within the period, and they certainly need not adhere to homogenization [37,38]. Second, the MMARC can be applied *after-the-fact* to perfect the performance of suboptimal structures, being an independent superstrate module employed without any modification to the original BPS. In this sense, the MMARC can be considered as complementing metasurfaces or metagratings, since the MMARC can be designed to perfect them in cases of inferior performance. Third, since the BPS is given and only then the MMARC is designed to obtain the desired effect, the BPS is essentially "decoupled" from the design, affecting only the properties of the MMARC. This is in contrast to standard devices in which all components of the structure participate in the design simultaneously. Lastly, and perhaps most importantly, the elementary wave physics employed in propagation through layered media, on which MMARC synthesis relies, makes this solution applicable to a wide variety of physical systems, ranging from electromagnetic and optical devices to acoustic components and seismic scenarios.

Before tackling analytical aspects of the MMARC, we emphasize again that the MMARC concept is not associated with a specific BPS, nor with a metasurface, nor with a metagrating. Instead, it represents a new path towards manipulating fields by merely adjusting the properties of homogeneous slabs, a process that is universally applicable to any wave-based discipline. *Only* these slabs are adjusted; there is no tailored periodic configuration that participates in the design as would be required in metasurface and metagrating synthesis. It is this modular and generally applicable enhancement approach which, as mentioned above, could certainly complement metasurface and metagrating (as well as other BPS) design. This essence of the MMARC concept is expected to provide fresh insights and a useful framework for synthesizing alternative wave-deflecting systems.

## II. ANALYTICAL MODEL

To facilitate this concept and showcase its merits, we begin by devising an efficient analytical model for determining the characteristics of the uniform dielectric layers of the MMARC needed to obtain desired anomalous effects. This model would calculate the fields scattered from the BPS-MMARC combination for different layer configurations, and would employ parametric variation schemes to choose an optimum configuration. Consider, then, a BPS that is invariant in the $z$ direction with periodicity $d$ along $x$, coated below by a metallic layer to assure reflection (Fig. 1). For transverse magnetic (TM) polarization, the magnetic field $\mathbf{H} = H_z \hat{\mathbf{z}}$, while the electric field $\mathbf{E}$ will not contain a $z$ component. The BPS is coated above by a MMARC consisting of $M$ dielectric layers, where layer $m$ is characterized by dielectric constant $\epsilon_r^{(m)}$ and thickness $h^{(m)} = y^{(m)} - y^{(m-1)}$. In accordance with the Floquet-Bloch (FB) theorem, a plane wave $H_{z,\mathrm{inc}}(x, y) = H_0 e^{ik_{x0}x} e^{-ik_{y0}^{(M+1)}y}$ incident in region $M + 1$ on the BPS-MMARC system at an angle $\theta_{\mathrm{inc}}$ will be scattered into a discrete spectrum of (propagating and evanescent) waves,

$$H_z^{(M+1)}(x, y) = H_{z,\mathrm{inc}} + \sum_{p=-\infty}^{\infty} \rho_p e^{ik_{xp}x} e^{ik_{yp}^{(M+1)}y}, \quad y > y^{(M)}, \quad (1)$$

and the transverse and longitudinal wavenumbers of the $p$th mode in the $m$th layer are given, respectively, by

$$k_{xp} = k\sin\theta_{\mathrm{inc}} + 2p\pi/d, \quad k_{yp}^{(m)} = \left(k^{(m)2} - k_{xp}^2\right)^{1/2}. \quad (2)$$

$d = \lambda/|\sin\theta_{\mathrm{ref}} - \sin\theta_{\mathrm{inc}}|$ is the BPS periodicity, $\theta_{\mathrm{ref}}$ is the design anomalous reflection angle given by the $p = 1$ value of

$$\cos\theta_p = \frac{k_{yp}^{(M+1)}}{k^{(M+1)}} = \frac{\sqrt{k^2 - k_{xp}^2}}{k}, \quad (3)$$

the wave number $k = 2\pi/\lambda$, $\lambda$ is the wavelength in free space, $k^{(m)} = k[\epsilon_r^{(m)}]^{1/2}$ is the wave number in layer $m$, an $e^{-i\omega t}$ time dependence is assumed, and the modal reflection coefficients $\rho_p$ are, as yet, unknown.

In order to keep the geometry simple, normal incidence ($\theta_{\mathrm{inc}} = 0$) will be assumed, along with $\theta_{\mathrm{ref}} > 30°$, which lead to three values of $p$ for which $k_{yp}$ is real: $p = [-1, 0, 1]$ [13], corresponding to waves propagating towards $\theta_p = [-\theta_{\mathrm{ref}}, 0, \theta_{\mathrm{ref}}]$ (red arrows in Fig. 1); all other terms in Eq. (1) represent evanescent waves. The goal of the analytical model is to determine the efficiencies $\eta_p^\rho = |\rho_p|^2 \cos\theta_p/\cos\theta_{\mathrm{inc}}$ with which power is coupled from the incident wave to each of the scattered waves. Straightforward optimization algorithms can then be employed to determine, say, the $h^{(m)}$ for which perfect anomalous reflection is attained: $\eta_{-1}^\rho \to 0$, $\eta_0^\rho \to 0$, $\eta_1^\rho \to 1$.

Formulation of the analytical model will be facilitated by employing an auxiliary air region of thickness $h^{(0)}$ between the BPS and the MMARC (Fig. 2). Eventually, to match the actual configuration, the limit $h^{(0)} \to 0$ will be taken. The mixing of the Floquet-Bloch modes is assumed to occur within this air region by virtue of the periodicity along its lower boundary. It is worth noting that this is different from a configuration in which the auxiliary region material itself varied periodically [39], the latter being incompatible with
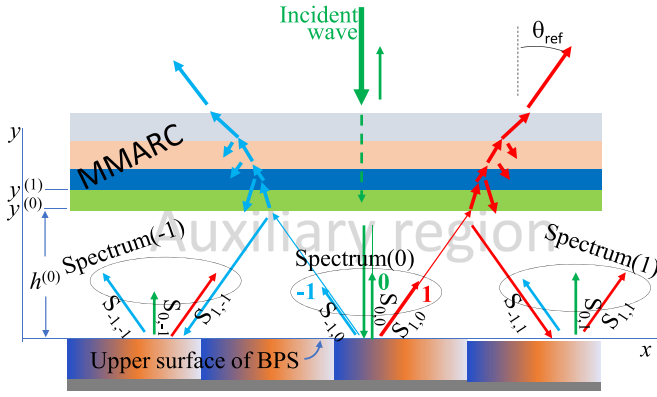
FIG. 2. FB wave interactions in an auxiliary region between the MMARC and the BPS. In these interactions, multiply-reflected waves $-1$, 0, and 1 (corresponding to the FB indices of propagating waves in Fig. 1) produce FB discrete Spectrum($-1$), Spectrum(0), and Spectrum(1). The components of these spectra are related to the terms $S_{p,q}$ of the scattering matrix.

decoupling the mixing region from the adjacent MMARC layers.

The general solutions for the $H$ field in the $m$th MMARC layer and in the auxiliary ($m = 0$) region are

$$H_z^{(m)}(x, y) = \sum_{p=-\infty}^{\infty} e^{ik_{xp}x} \left[ A_p^{(m)} e^{-ik_{yp}^{(m)}y} + B_p^{(m)} e^{ik_{yp}^{(m)}y} \right],$$

$$y^{(m-1)} < y \leqslant y^{(m)}, 0 \leqslant m \leqslant M, \qquad (4)$$

where $y^{(-1)} \equiv 0$. Each term in the sum represents a superposition of a downward wave (the $A_p^{(m)}$ term) and an upward wave (the $B_p^{(m)}$ term) which satisfy the Helmholtz equation in each layer. The unknown coefficients $A_p^{(m)}$, $B_p^{(m)}$, $\rho_p$ may be determined from the boundary conditions that require continuity of $H_z^{(m)}$ and $E_x^{(m)} = [iZ/(k\epsilon_r^{(m)})] \partial H_z^{(m)}/\partial y$ across each interface, where $Z$ is the impedance of free space. The detailed expressions for $E_x^{(m)}$ are derived in Appendix A as Eqs. (A8), (A9), and the boundary conditions are given in Eqs. (A14) to (A17). For layers $m > 0$ above the auxiliary region, owing to the orthogonality of the $e^{ik_{xp}x}$ functions over the period $d$, these boundary conditions are satisfied *separately* for each specific FB mode $p$. However, these modes are coupled to each other in the auxiliary region.

From Eq. (4), the $H$ field in the auxiliary region $m = 0$, above the BPS, is

$$H_z^{(0)}(x, y) = \sum_{p=-\infty}^{\infty} e^{ik_{xp}x} \left[ A_p^{(0)} e^{-ik_{yp}^{(0)}y} + B_p^{(0)} e^{ik_{yp}^{(0)}y} \right], 0 \leqslant y \leqslant y^{(0)}.$$

$$(5)$$

Because of the periodicity of the lower boundary (BPS) of the auxiliary region, an additional condition is required in that region which serves to describe the coupling of the modes one to another. This additional condition will be derived with the aid of a ray optics model. Although the rays in this model can only represent propagating waves, the generalization to include evanescent waves will be made clear below. Consider, then, the downward incident ray of Fig. 2 (green) that has

propagated through the MMARC and the auxiliary region. We know that this ray is scattered by the BPS into Spectrum(0) of multiple Floquet-Bloch (FB) rays, with the three propagating rays labeled by their FB indices $-1$, 0, and 1. For example, ray 1 (red) may be traced upward to the MMARC. While a branch of this ray will be transmitted back through the MMARC to the incidence region, another branch will be reflected from the MMARC back to the BPS where it will again be multiply-scattered from the BPS into Spectrum(1). Although the rays of Spectrum(1) are in the directions of the rays of Spectrum(0), their magnitudes and phases will be different since they were excited by "incident" rays in different directions. This would be the case, as well, for Spectrum($-1$) which is excited by ray $-1$ (cyan), and for Spectrum(0) which is excited by ray 0 (green). It is clear, then, that the wave in the auxiliary region that is propagating, say, in direction 1 is composed of contributions from downward "incident" waves in the $-1$, 0, and 1 directions. If these "incident" wave amplitudes were unitary, then these contributions would simply be the terms $S_{1,-1}$, $S_{1,0}$, $S_{1,1}$ of the scattering matrix referenced to the origin ($x = 0$, $y = 0$) of our coordinate system (see Fig. 2). Since these "incident" wave amplitudes are instead $A_{-1}^{(0)}$, $A_0^{(0)}$, $A_1^{(0)}$, the amplitude of the wave reflected in the 1 direction from the surface at $x = 0$, $y = 0$ would satisfy

$$B_1^{(0)} e^{ik_{x,1}x} e^{ik_{y,1}^{(0)}y} = S_{1,-1} A_{-1}^{(0)} e^{ik_{x,-1}x} e^{-ik_{y,-1}^{(0)}y} + S_{1,0} A_0^{(0)} e^{ik_{x,0}x} e^{-ik_{y,0}^{(0)}y}$$

$$+ S_{1,1} A_1^{(0)} e^{ik_{x,1}x} e^{-ik_{y,1}^{(0)}y}, x = 0, y = 0 \qquad (6)$$

or more generally

$$B_p^{(0)} = \sum_{q=-\infty}^{\infty} S_{pq} A_q^{(0)}. \qquad (7)$$

The $S_{qp}$ are essentially the S parameters de-embedded to the origin (0,0). It is important to note that Eq. (7) is related to the region $m = 0$, or the "auxiliary" region which is composed of air. It was important to define this region as consisting of air, since it is only for such a background region that the S parameters are defined in the full wave computation programs. Even if the thickness $h^{(0)}$ of the auxiliary region is 0 as in Fig. 1(b), Eq. (7) still holds.

The result in Eq. (7) is not limited to the propagating rays used for demonstration purposes in Fig. 2; it includes evanescent waves as well, which we have found to be essential for the fidelity of the model. For some surfaces, the $S_{pq}$ can be found in closed form [18,19,31,34,35,38]; otherwise, they are readily provided by full-wave commercial programs as byproducts of their solution for scattering from a periodic surface [40]. Hence, we consider them as known for a given BPS, and use them as our starting point for designing the MMARC. This further highlights the modularity of our solution: Various MMARCs can be considered for the same BPS without requiring recalculation of these $S_{pq}$ parameters.

As detailed in Appendix A 4, by truncating the infinite sums in Eqs. (1), (4), and (7) to sums from $-P$ to $P$ ($P = 2$ was found to yield sufficient accuracy for our analytical results), the boundary conditions provide the same number of equations as the number of unknown coefficients. (Note that even after the truncation, several evanescent modes are included in the analysis.) After letting $h^{(0)} \to 0$, this would

permit all of the unknowns to be found as a solution to a linear system of simultaneous equations (Appendix A 4), and in particular the coupling efficiencies $\eta_p^\rho$ that we wish to optimize for anomalous reflection.

For a given BPS (which generally would not provide the sought-for anomalous reflection), these $\eta_p^\rho$ are clearly related to the physical characteristics of the MMARC. In particular, and as mentioned earlier, the modes' cumulative propagation throughout the stratified media, and interaction with the BPS, would determine the result of the modal interference in free space. For simplicity, and because not all substrate materials are commercially available, it will be assumed that the material properties $\epsilon_r^{(m)}$ of each layer, and the number of layers $M$, are given, so that $\eta_p^\rho = \eta_p^\rho(h^{(m)})$, $1 \leqslant m \leqslant M$. We utilize this formulation as a basis for solving the inverse problem: determination of the MMARC layer thicknesses $h^{(m)}$ which provide the sought-for anomalous reflection values of $\eta_p^\rho$, accomplished via a simple parametric-sweep-based algorithm (see Appendix B).

We note that although the presented formalism utilizes simple ray optics, this approach rigorously captures the essence of a given BPS without requiring details of its underlying structure. This observation forms an important building block in facilitating the universal and modular nature of the proposed solution, and could indeed be useful for similar wave analyses in other physical domains.

## III. RESULTS AND DISCUSSION

To demonstrate the proposed scheme and highlight its versatility, we utilize it to realize MMARCs for various types of BPSs and anomalous reflection functionalities. It is clear that each additional layer in the MMARC provides an additional degree-of-freedom $h^{(m)}$ for attaining the desired anomalous reflection. Since the $\epsilon_r^{(m)}$ are often limited by available inventory, we constrain ourselves to two types of low-loss printed-circuit-board (PCB) substrate materials, arranged in alternate layers: Rogers RO3010 ($\epsilon_r = 10.2$) and RO3003 ($\epsilon_r = 3$) [41]. All configurations will be investigated for a reflection angle $\theta_{\text{ref}} = 70°$ and a frequency of 20 GHz. It is apparent, though, that the methodology is entirely applicable to waves in any portion of the electromagnetic spectrum.

Several types of BPS will be considered in this section. These include printed circuit boards (PCBs) with periodically distributed metallic strips, blazed surfaces, arrays of shorted parallel plate waveguides, and periodic arrays of multiple dielectrics. This will demonstrate the universal capability of a MMARC to produce perfect anomalous reflection, independent of the type of BPS to which it is applied.

### A. Versatile diffraction engineering

We consider first the simple BPS of Fig. 3 consisting of three metal strips of different widths printed on a grounded dielectric substrate $\epsilon_r = 3$. This configuration is typical of many recent metasurfaces and metagratings (especially at microwave frequencies), thus forming a representative case study for practical applications [28,29,42–45]. As part of the BPS, we protect the metal strips from above by an additional
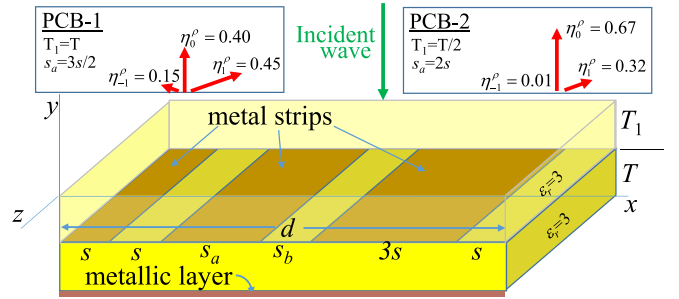


FIG. 3. One period of a BPS consisting of three metal strips of widths $s$, $s_a$, $3s$ printed on a grounded dielectric substrate of thickness $T = 60$ mil $\approx 1.524$ mm that is covered by a dielectric substrate with the same material of thickness $T_1$. $s = d/9$, $s_b = 3s - s_a$. Also shown are the full-wave-calculated mode-coupling results for this BPS alone (i.e., without a MMARC), for two sets of values of $T_1$ and $s_a$.

substrate with the same dielectric constant. This also plays the role of distancing the upper face of the BPS from the thin-metal-induced evanescent waves of higher order, thereby maintaining the validity of the truncation of Eq. (4) which accounts only for low-order evanescent modes [46]. Two configurations are considered for the BPS in Fig. 3, denoted as PCB-1 and PCB-2 in the figure. These differ in the specific dimensions of both the metallic strips and the protective cover. The corresponding coupling efficiencies $\eta_p^\rho = |S_{p0}|^2$ are shown as well in the inset. It should be emphasized that the size and locations of the metallic strips in Fig. 3 were chosen with no operational goal whatsoever. For the PCB-1 configuration, for example, the strip widths are simply $s$, $2s$, and $3s$ with a separation of $s$. The fact that a MMARC will be found to produce perfect anomalous reflection from such a simple BPS will demonstrate the versatility of the method.

Since the BPS alone does not produce perfect anomalous reflection ($\eta_1^\rho = 0.45$ for PCB-1 and $\eta_1^\rho = 0.32$ for PCB-2), it is desired to find a MMARC to coat the BPS so that the combined structure achieves $\eta_1^\rho \rightarrow 1$, $\eta_{-1}^\rho = \eta_0^\rho \rightarrow 0$. The PCB-1 configuration for the BPS shown in Fig. 3 is first considered for $M = 3$ [Figs. 4(a) and 4(c)] and $M = 5$ [Figs. 4(b) and 4(d)] MMARC layers. Resolving the optimal layer dimensions based on the model and methodology outlined in Sec. II (see also Appendix B) leads to the enhanced BPS-MMARC configurations and resulting anomalous reflection performance shown in Figs. 4(a) and 4(b): $h^{(m)}/\lambda = [0.452, 0.225, 0.104]$, $\eta_1^\rho = 0.94$ for $M = 3$; $h^{(m)}/\lambda = [0.02, 0.04, 0.08, 0.15, 0.01]$, $\eta_1^\rho = 0.99$ for $M = 5$. Indeed, as apparent from the plots, utilizing more degrees of freedom (larger $M$) may lead to improved solutions, providing $\eta_1^\rho$ values closer to unity for smaller overall thicknesses. The success of the analytical model may be seen in Figs. 4(c) and 4(d) which compare its $H_z(x, y)$ results to those of CST in each of the media for these two MMARCs [47]. For each configuration, the presence of surface waves (white arrows) is apparent. Such surface waves, which are implicitly excited by our BPS-MMARC solution, had to be specifically designed into previous solution methods [13,48].
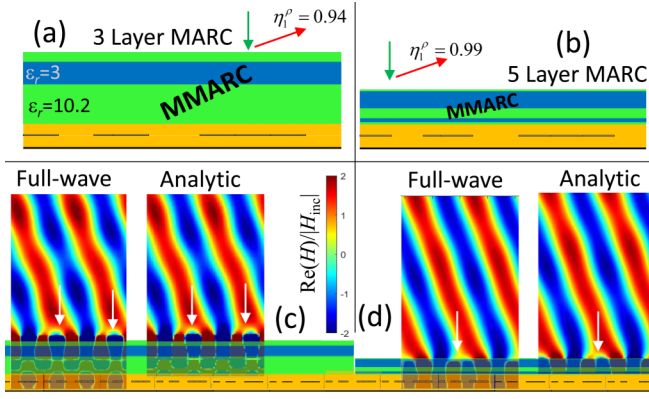
FIG. 4. Anomalous reflection solutions for $M = 3$-layer [(a) and (c)] and $M = 5$-layer [(b) and (d)] MMARC configurations, PCB-1 BPS of Fig. 3. [(a),(b)] The MMARC layers and anomalous reflection results. [(c),(d)] $H_z(x, y)$ as computed by the analytical model and by full-wave CST simulations. Green and blue layers in the MMARC correspond to Rogers RO3010 ($\epsilon_r = 10.2$) and RO3003 ($\epsilon_r = 3$), respectively.
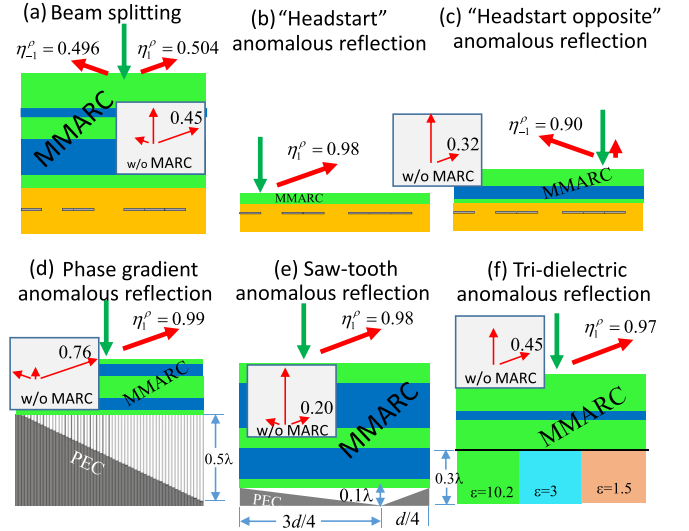


FIG. 5. MMARC for various purposes and surface types. For each case, the full-wave-calculated FB spectrum without the MMARC is shown as an inset that includes the numerical value of $\eta_1^\rho$. The FB spectrum with the MMARC is shown above the MMARC. (a) Beam splitting, PCB-1 BPS of Fig. 3; $h^{(m)} = [0.06, 0.16, 0.11, 0.03, 0.18]\lambda$. (b) "Headstart" anomalous reflection, PCB-2 BPS of Fig. 3; $h^{(1)} = 0.058\lambda$. (c) "Headstart" opposite-direction anomalous reflection, same BPS as (b); $h^{(m)} = [0.026, 0.078, 0.107]\lambda$. (d) Anomalous reflection, phase-gradient BPS; $h^{(m)} = [0.025, 0.075, 0.125, 0.075, 0.025]\lambda$. (e) Anomalous reflection, bilinear sawtooth-shaped BPS; $h^{(m)} = [0.053, 0.179, 0.109, 0.255, 0.094]\lambda$. (f) Anomalous reflection, tri-dielectric BPS; $h^{(m)} = [0.161, 0.054, 0.211]\lambda$.

The excellent agreement between the analytical predictions and the full-wave computations in Fig. 4 demonstrates the ability to design a MMARC to coat a simple, arbitrarily chosen periodic surface in order to produce the desired anomalous reflection.

The potpourri of BPS-MMARC configurations in Fig. 5 provides insight into the diversity of functionality and BPS-types to which the MMARC may be applied. For example, just as MMARCs coated a BPS in Fig. 4 to produce perfect anomalous reflection in the $\theta_{\text{ref}}$ direction, Fig. 5(a) displays a MMARC coating the *same* BPS to produce a beam that is "perfectly" split into the $\pm\theta_{\text{ref}}$ directions.

The BPS in Figs. 5(b) and 5(c) is the PCB-2 BPS configuration of Fig. 3, so that for the bare BPS, $\eta_{-1}^\rho \approx 0$ which is one of the requirements for anomalous reflection. It might be expected that using this BPS would provide a "headstart" for anomalous reflection, and that a relatively simple MMARC would suffice. Such a simple MMARC is indeed shown in Fig. 5(b), where only a single layer of relatively minute thickness $0.058\lambda$ provides the anomalous reflection $\eta_1^\rho = 0.97$. It should be emphasized, though, that this starting point does not prevent us from devising a MMARC that would actually reverse the direction of the original beam to the $\eta_{-1}^\rho$ direction. This stems from contributions to $\eta_{-1}^\rho$ from waves in other directions that only exist in the presence of the MMARC (see Fig. 2). To demonstrate this, Fig. 5(c) displays a MMARC, synthesized using the methodology described above, which coats the same PCB-2 BPS, and produces $\eta_{-1}^\rho = 0.90$; almost enough to be considered *oppositely-directed* anomalous reflection! That is, instead of a "standard" design target $\eta_1^\rho = 1$ for which the reflection angle is 70°, the MMARC succeeded in directing the reflection to −70°, this despite the fact that without the MMARC the BPS produced practically no wave in that direction.

It should be emphasized that the MMARC can provide solutions for *any* type of periodic surface, including complex surfaces composed of many meta-atoms. Figure 5(d) displays

a phase-gradient metasurface consisting of an array of parallel plate waveguides of different lengths [49,50] which, like any phase-gradient metasurface, is incapable of perfect anomalous reflection [16,51]. By itself, this structure produces $\eta_1^\rho = 0.76$. Coating it with the MMARC produces the impressive anomalous reflection $\eta_1^\rho = 0.99$. Figure 5(e) demonstrates that the BPS on which the MMARC is placed need not be smooth. It displays one period of a saw-tooth-shaped conducting surface with a MMARC that again produces perfect anomalous reflection ($\eta_1^\rho = 0.98$). Finally, Fig. 5(f) demonstrates that the MMARC solution also works well for a dielectric-based BPS, yielding perfect anomalous reflection ($\eta_1^\rho = 0.97$) for the given "tri-dielectric" composite. For each configuration above, the optimum layer thicknesses and $\eta_p^\rho$ values found by the analytical model differed by less than 1% from the full-wave results, verifying the formulation's fidelity.

The simulations described above assumed that any metal in the BPS is zero-thickness PEC, and the dielectrics are lossless. If 0.5 oz. copper with realistic conductivity is employed instead [41], the full-wave-calculated result remains effectively unchanged. Frequency response and material losses effects for BPS-MARC configurations in Figs. 4 and 5 are detailed in Appendix C. It is shown there that while dielectric loss may naturally pose a greater challenge to our scheme, considering its reliance on multiple reflections within the dielectric stack, this can be mostly mitigated by proper inclusion of the expected loss into the analytical model itself (see Appendix C 1).
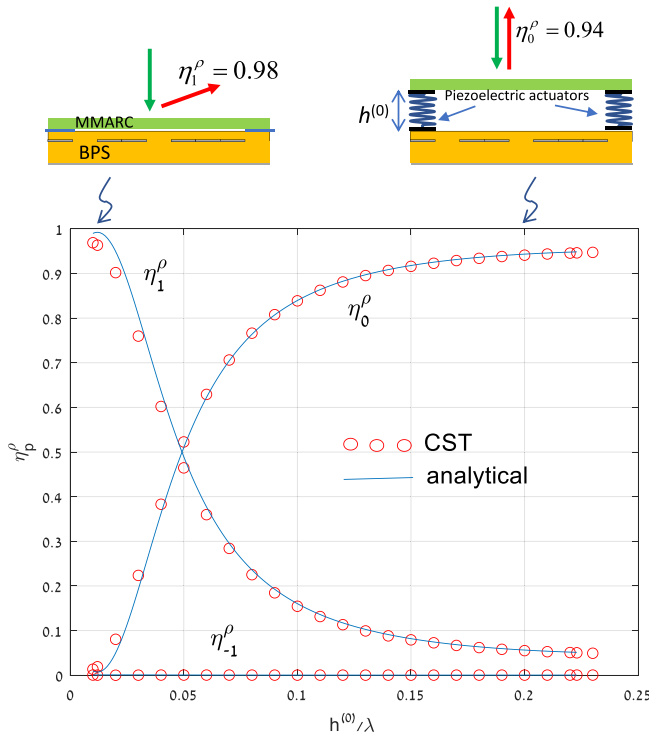
FIG. 6. The fraction $\eta_p^\rho$ of power coupled from the incident wave to each propagating FB wave as a function of the distance between the PCB-2 BPS of Fig. 3 and a single-layer MMARC of thickness $0.053\lambda$, dielectric constant 10.2.

### B. Dynamic beam switching

Most of the results discussed above dealt with MMARC design for anomalous reflection. It will be recalled that the analytical model presented in Sec. II was derived with the aid of an auxiliary region of thickness $h^{(0)} \rightarrow 0$, so that the final MMARC location was adjacent to the BPS. Clearly, since the MMARC principle relies on multiple reflections between different media, the extent of the air gap $h^{(0)}$ could have a profound effect on the scattering from the system. Indeed, for most cases, once the MMARC has been determined which produces perfect *anomalous* reflection for $h^{(0)} \approx 0$, that MMARC can be placed at a certain finite distance from the BPS (i.e., $h^{(0)}$ finite) to provide perfect *specular* reflection [52]. That is, the angle of perfect reflection of the beam can be switched by varying the distance of the MMARC from the BPS.

This tunability which can be realized with the aid of piezoelectric actuators that move the MMARC relative to the BPS [53–55], is applied to two BPS-MMARC combinations in Figs. 6 and 7. In each case, the power coupling efficiency $\eta_p^\rho$ for each index $p$ is plotted as a function of the separation distance $h^{(0)}$ between the MMARC and the BPS. In Fig. 6, the PCB-2 BPS is used (see Fig. 3) with a MMARC similar to that of Fig. 5(b), while in Fig. 7, the PCB-1 BPS is used with the MMARC of Fig. 4(b). Near the top of each figure, the configuration of the MMARC relative to the BPS is shown both for anomalous reflection and for specular reflection. In each figure, the horizontal locations of these configurations are near their respective $h^{(0)}$ values of the plot.
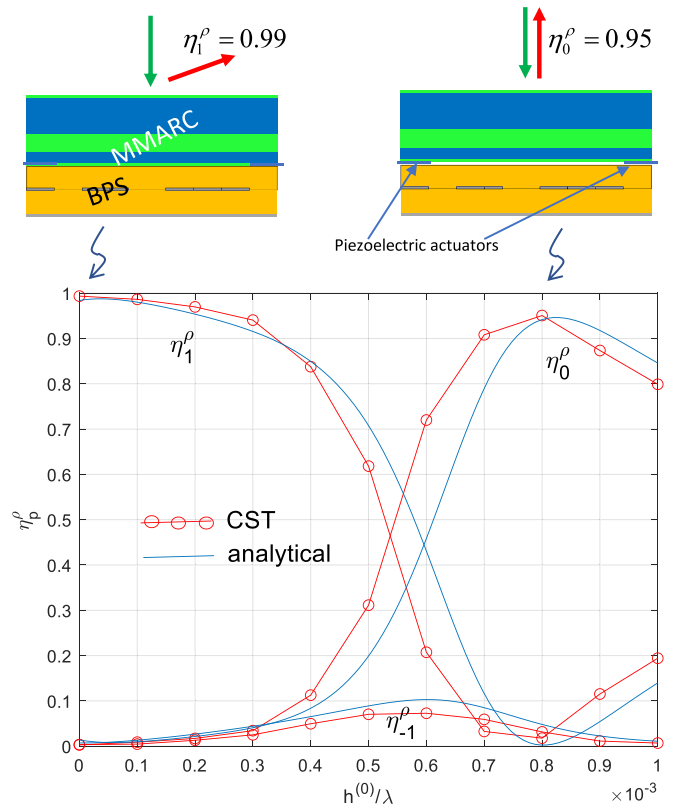


FIG. 7. The fraction $\eta_p^\rho$ of power coupled from the incident wave to each propagating FB wave as a function of the distance between the PCB-1 BPS of Fig. 3 and the five-layer MMARC of Fig. 4(b) with thicknesses $h^{(m)}/\lambda = [0.02, 0.04, 0.08, 0.15, 0.01]$.

We note that the MMARC-based steering mechanism can be devised with different levels of sensitivity, depending also on the underlying BPS. In particular, in Fig. 6, the change from anomalous reflection to specular reflection occurs over a distance $h^{(0)} \approx 0.2\lambda$, while in Fig. 7, that change occurs over a distance of only $0.8 \times 10^{-3}\lambda$. This provides a path towards integration of the proposed concept in a variety of applications and operating regimes, where the required offset distances with respect to the wavelength can be adapted to meet limitations of the available displacement mechanisms in practice. In spite of these sensitivity differences, the analytical predictions agree well with the full-wave results. The analytical method is therefore compatible with this beam switching method which does not rely on such nonlinear components as diodes that are associated with non-negligible losses [56–58], especially at high frequencies [59]. As before, since the principles are based on wave propagation through the layered MMARC, they would be applicable to any wave-based discipline, including these challenging spectral regions in the mm-wave, THz, and optical regimes.

### C. Experimental validation

Finally, to provide further support for the practical viability of the proposed concept, we have fabricated a BPS-MMARC prototype corresponding to that of Fig. 5(b) using commercially available laminates, and characterized it experimentally in a cylindrical near-field measurement setup. The details of
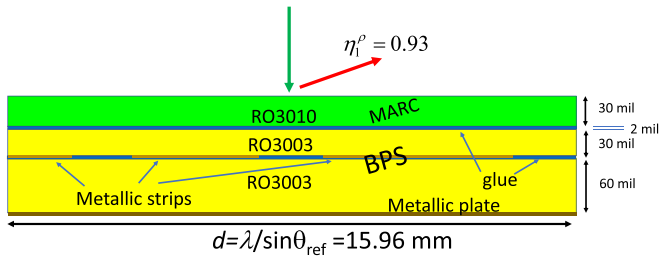
FIG. 8. One period of the BPS-MMARC device that was measured to demonstrate the practical viability of the MMARC concept. The coupling efficiency shown was computed by CST. 1 mil =.001 inch = 25.4μm.

this BPS-MMARC configuration are shown in Fig. 8, including the 2-mil thick ($\approx 0.0508$ mm) Rogers 2929 Bondply characterized by $\varepsilon_r = 2.94$, $\tan\delta = 0.003$ that was used to bond the substrates together. The thickness of the single-layer MMARC that was employed in the experiment is 30 mil $\approx 0.762$ mm, or $0.0508\lambda$ at 20 GHz, which is the closest commercially-available Rogers RO3010 laminate thickness to the optimal value of $0.058\lambda$ obtained via our approach [see Fig. 5(b)]. Note that these minor differences due to realistic implementation considerations (dimensions, loss), have affected mildly the overall device efficiency, now predicted in simulations to exhibit a 93% anomalous reflection efficiency (Fig. 8) compared to the original 97% of Fig. 5(b). Nonetheless, these figures of merit still exhibit a dramatic improvement with respect to the original BPS, by a factor of $\approx 2.8$.

For comparison, scattering patterns from two prototypes were measured; one from the BPS alone (PCB-1 BPS, Fig. 3), and the other from the MMARC-enhanced BPS device (Fig. 8). Each prototype measured 30 cm × 22.5 cm $\approx 20\lambda \times 15\lambda$, fabricated using standard PCB manufacturing procedures by *PCB Technologies Ltd*. The cylindrical near-field measurements [35] were performed in our anechoic chamber (MVG/Orbit-FR) using the setup shown in Fig. 9. The device-under-test (DUT) was mounted on a foam stand at a fixed distance $D = 43$ cm $\approx 28.6\lambda$ from the Gaussian beam antenna (Millitech, Inc., GOA-42-S000094). A metal
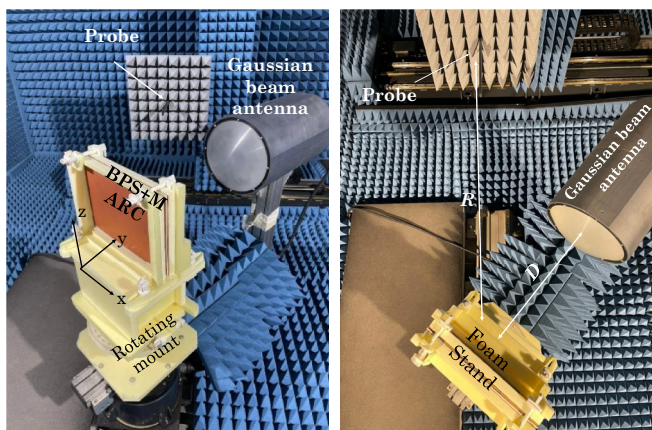


FIG. 9. Experimental setup for measuring the scattering patterns of the BPS-MMARC device.
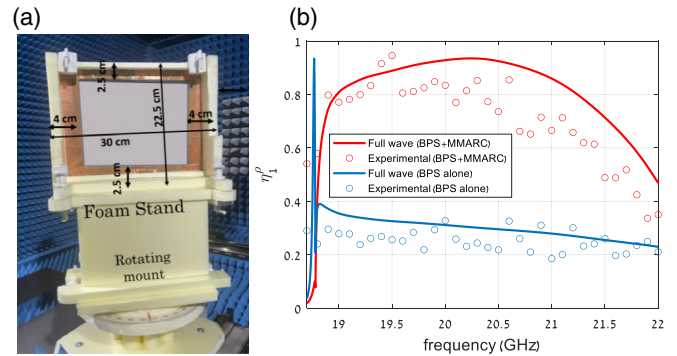


FIG. 10. Experimentally measured frequency response for the configuration of Fig. 8. (a) Metal frame to prevent unwanted transmissions. (b) Simulated (solid) and measured (circles) $\eta_1^\rho$ with (red) and without (blue) the MMARC. The lowest frequency in the plot is near the cutoff frequency for the plotted mode.

frame with internal dimensions 22 cm × 17.5 cm $\approx 14.67\lambda \times 11.67\lambda$ was fastened to the stand in front of the DUT, to prevent unwanted transmissions through the unpatterned edges of the fabricated boards from hindering the measurements [see Fig. 10(a)]. This $14.67\lambda$ dimension was sufficient to expose about 9 periods of the BPS-MMARC device of Fig. 8 to the Gaussian beam illumination. An open-ended waveguide nearfield probe is located at a horizontal distance $R = 79$ cm $\approx 52.67\lambda$ from the DUT. The measurement is carried out with the aid of a data acquisition module programed to azimuthally rotate the DUT and the Gaussian beam antenna together from $-145°$ to $145°$ relative to the probe which is moved up and down periodically. Thus, the probe effectively measures the field over a cylindrical surface of radius $R$, the vertical axis of which is centered at the prototype. This recorded nearfield data is finally postprocessed with MiDAS data acquisition and analysis software to produce the desired far-field pattern based on the equivalence principle.

The measurements performed on the DUT were repeated with the DUT removed, but with the limiting metal frame in place. This provided a reference radiation pattern of the Gaussian beam antenna, allowing the calculation of total incident power on the DUT required for efficiency calculations. All the measurements were performed in the frequency range of 18 GHz to 22 GHz. The measured coupling efficiency for mode $p$ at frequency $f$ was evaluated via [34],

$$\eta_p^\rho(f) = \frac{G_p(f)}{G_{\text{ref}}(f)} \frac{1}{\cos\theta_p}, \quad (8)$$

where $G_{\text{ref}}(f)$ denotes the measured reference gain (i.e., without the DUT) in the incidence ($\theta_{\text{in}} = 0$) direction for frequency $f$, and $G_p(f)$ denotes the gain of the wave scattered from the DUT in the direction $\theta_p$ of Floquet-Bloch mode $p$ [see Eq. (3)]. This produced the measured frequency responses for $p = 1$ given in Fig. 10(b).

Comparing in Fig. 10(b) the full-wave simulated (solid) and experimentally measured (circles) $\eta_1^\rho$ as a function of frequency for the bare BPS (blue) and the MMARC-enhanced device (red) clearly shows the substantial boost in anomalous reflection efficiency facilitated by the MMARC superstrate. The measured and simulated results display the same

broadband behavior, providing further evidence of the veracity of our approach. This relatively broadband behavior may derive from the structural simplicity of only a single MMARC layer (see Fig. 8). It is apparent that the MMARC-enhanced measured coupling efficiency is about 10% lower than the CST-simulated efficiency. (This number fluctuates a bit over the measured frequency range.) We associate this discrepancy with material parameter tolerances of the DUT. Indeed, it was found that if the permittivity of the simulated BPS and MMARC materials were reduced by 10% (a plausible possibility considering previously reported permittivity variations of similar Rogers laminates [60–62]), the simulated efficiency would agree with the measured efficiency. Overall, we conclude that the MMARC performs well across the band, increasing the measured (simulated) fraction of incident power coupled to the anomalous mode from $\eta_1^\rho = 0.33$ ($\eta_1^\rho = 0.31$) to $\eta_1^\rho = 0.83$ ($\eta_1^\rho = 0.93$) at the design frequency, thus validating our concept.

## IV. CONCLUSION

In summary, we have shown that multimodal antireflective coatings (MMARCs) can be designed for arbitrary types of periodic surfaces (BPS) to achieve perfect or near-perfect anomalous reflection effects. Despite the simplicity of the concept, we have demonstrated theoretically and experimentally that such a rudimentary stack of homogeneous layers can interfere strongly enough with the complex diffraction pattern of the BPS to significantly change its spectral behavior. This conclusion is not trivial, and reveals a mechanism of interlaced Fabry-Perot resonators. The proposed modular solution, circumventing the need for high-resolution structural engineering, merely requires utilization of multiple reflections in slabs with different wave velocities. Thus, it is expected to allow similar "corrections" to beam deflecting devices in other physical fields dominated by wave phenomena, e.g., acoustics or seismics, and provide an appealing route to enhance applications in frequency regimes where subwavelength fabrication is challenging (optics, x-rays).

## APPENDIX A: ANALYTICAL DERIVATIONS

### 1. The *H* field

For TM polarization, the *H* field is in the *z* direction. In the uppermost $(M + 1)$ region, this field is given by Eq. (1), and in the other regions *m*, this field is given by Eq. (4). The $\rho_p$ in Eq. (1) and the $A_p^{(m)}, B_p^{(m)}$ in Eq. (4) are unknowns to be determined by satisfying the boundary conditions. Equation (1) can be placed in the form of Eq. (4) by recalling that it relates to region number $m = M + 1$, letting $\rho_p = B_p^{(M+1)}$, and setting $A_p^{(M+1)} = 0$. Then Eq. (1) becomes

$$H_z^{(M+1)}(x, y) = H_0 e^{ik_{x0}x} e^{-ik_{y0}^{(M+1)}y}$$
$$+ \sum_{p=-\infty}^{\infty} B_p^{(M+1)} e^{ik_{xp}x} e^{ik_{yp}^{(M+1)}y}, y > y^{(M)}. \tag{A1}$$

### 2. Derivation of the *E* field

In general, the *E* field in medium *m* may be found from

$$\mathbf{E}^{(m)} = \frac{iZ}{k\varepsilon_r^{(m)}} \nabla \times \mathbf{H}^{(m)}, \tag{A2}$$

where $Z = \sqrt{\mu_0/\varepsilon_0}$ is the impedance of free space, and $\mu_0, \epsilon_0$ are the permeability and permittivity of free space. We will be interested in the *x* component of $\mathbf{E}^{(m)}$ since that is the component parallel to the material interfaces. In medium *m*, since there is only a *z* component of $\mathbf{H}$,

$$E_x^{(m)}(x, y) = Z \sum_{p=-\infty}^{\infty} e^{ik_{xp}x} C_p^{(m)} \left[ A_p^{(m)} e^{-ik_{yp}^{(m)}y} - B_p^{(m)} e^{ik_{yp}^{(m)}y} \right], \tag{A3}$$

where

$$C_p^{(m)} \equiv \frac{k_{yp}^{(m)}}{k\varepsilon_r^{(m)}}. \tag{A4}$$

Then

$$E_x^{(M+1)}(x, y) = ZC_0^{(M+1)} H_0 e^{ik_{x0}x} e^{-ik_{y0}^{(M+1)}y}$$
$$- Z \sum_{p=-\infty}^{\infty} C_p^{(M+1)} B_p^{(M+1)} e^{ik_{xp}x} e^{ik_{yp}^{(M+1)}y}. \tag{A5}$$

The field equations (4), (A1), (A3), and (A5) may be summarized as

$$H_z^{(m)}(x, y) = \sum_{p=-\infty}^{\infty} e^{ik_{xp}x} \left[ A_p^{(m)} e^{-ik_{yp}^{(m)}y} + B_p^{(m)} e^{ik_{yp}^{(m)}y} \right],$$
$$y^{(m-1)} \leqslant y \leqslant y^{(m)}, 0 \leqslant m \leqslant M, \tag{A6}$$

$$H_z^{(M+1)}(x, y) = H_0 e^{ik_{x0}x} e^{-ik_{y0}^{(M+1)}y}$$
$$+ \sum_{p=-\infty}^{\infty} B_p^{(M+1)} e^{ik_{xp}x} e^{ik_{yp}^{(M+1)}y}, y > y^{(M)}, \tag{A7}$$

$$E_x^{(m)}(x, y) = Z \sum_{p=-\infty}^{\infty} e^{ik_{xp}x} C_p^{(m)} \left[ A_p^{(m)} e^{-ik_{yp}^{(m)}y} - B_p^{(m)} e^{ik_{yp}^{(m)}y} \right],$$
$$y^{(m-1)} \leqslant y \leqslant y^{(m)}, 0 \leqslant m \leqslant M, \tag{A8}$$

$$E_x^{(M+1)}(x, y) = ZC_0^{(M+1)} H_0 e^{ik_{x0}x} e^{-ik_{y0}^{(M+1)}y}$$
$$- Z \sum_{p=-\infty}^{\infty} C_p^{(M+1)} B_p^{(M+1)} e^{ik_{xp}x} e^{ik_{yp}^{(M+1)}y}, y > y^{(M)}. \tag{A9}$$

### 3. The boundary conditions: Material interfaces

The boundary conditions require that the tangential component of each field be continuous across each interface $y = y^{(m)}$,

$$H_z^{(m)}(x, y^{(m)}) = H_z^{(m+1)}(x, y^{(m)}), 0 \leqslant m \leqslant M, \tag{A10}$$

$$E_x^{(m)}(x, y^{(m)}) = E_x^{(m+1)}(x, y^{(m)}), 0 \leqslant m \leqslant M. \tag{A11}$$

The boundary condition along the top of the BPS at $y = 0$ will be discussed below. It is desired to utilize these boundary conditions in the form of a linear system of simultaneous equations that can be solved for the unknowns $A_p^{(m)}, B_p^{(m)}$. Using Eq. (A6) in Eq. (A10) yields

$$\sum_{p=-\infty}^{\infty} e^{i2\pi px/d} \left[ A_p^{(m)} e^{-ik_{yp}^{(m)} y^{(m)}} + B_p^{(m)} e^{ik_{yp}^{(m)} y^{(m)}} - A_p^{(m+1)} e^{-ik_{yp}^{(m+1)} y^{(m)}} - B_p^{(m+1)} e^{ik_{yp}^{(m+1)} y^{(m)}} \right] = 0, \, 0 \leqslant m \leqslant M-1, \tag{A12}$$

where Eq. (2) was used. Using Eq. (A6) and Eq. (A7) in Eq. (A10) yields

$$\sum_{p=-\infty}^{\infty} e^{i2\pi px/d} \left[ A_p^{(m)} e^{-ik_{yp}^{(m)} y^{(m)}} + B_p^{(m)} e^{ik_{yp}^{(m)} y^{(m)}} - B_p^{(m+1)} e^{ik_{yp}^{(m+1)} y^{(m)}} \right] = H_0 e^{-ik_{y0}^{(m+1)} y^{(m)}}, \, m = M. \tag{A13}$$

But these equations must hold separately for the different orders of $e^{i2\pi x/d}$. Therefore, Eqs. (A12) and (A13) may be written

$$A_p^{(m)} e^{-ik_{yp}^{(m)} y^{(m)}} + B_p^{(m)} e^{ik_{yp}^{(m)} y^{(m)}} - A_p^{(m+1)} e^{-ik_{yp}^{(m+1)} y^{(m)}} - B_p^{(m+1)} e^{ik_{yp}^{(m+1)} y^{(m)}} = 0, \, 0 \leqslant m \leqslant M-1, \, -\infty < p < \infty, \tag{A14}$$

$$A_p^{(m)} e^{-ik_{yp}^{(m)} y^{(m)}} + B_p^{(m)} e^{ik_{yp}^{(m)} y^{(m)}} - B_p^{(m+1)} e^{ik_{yp}^{(m+1)} y^{(m)}} = \delta_{p0} H_0 e^{-ik_{y0}^{(m+1)} y^{(m)}}, \, m = M, \, -\infty < p < \infty, \tag{A15}$$

where $\delta_{pq}$ is the Kronecker delta function. These equations implement the continuity of the $H$ field across the material interfaces. The continuity of the $E$ field across these interfaces will now be addressed.

Using Eq. (A8) in Eq. (A11) yields

$$A_p^{(m)} C_p^{(m)} e^{-ik_{yp}^{(m)} y^{(m)}} - B_p^{(m)} C_p^{(m)} e^{ik_{yp}^{(m)} y^{(m)}} - A_p^{(m+1)} C_p^{(m+1)} e^{-ik_{yp}^{(m+1)} y^{(m)}} + B_p^{(m+1)} C_p^{(m+1)} e^{ik_{yp}^{(m+1)} y^{(m)}} = 0, \, 0 \leqslant m \leqslant M-1, \, -\infty < p < \infty. \tag{A16}$$

Using Eqs. (A8) and (A9) in Eq. (A11) yields

$$A_p^{(m)} C_p^{(m)} e^{-ik_{yp}^{(m)} y^{(m)}} - B_p^{(m)} C_p^{(m)} e^{ik_{yp}^{(m)} y^{(m)}} + B_p^{(m+1)} C_p^{(m+1)} e^{ik_{yp}^{(m+1)} y^{(m)}} = \delta_{p0} H_0 C_0^{(m+1)} e^{-ik_{y0}^{(m+1)} y^{(m)}}, \, m = M, \, -\infty < p < \infty. \tag{A17}$$

The interface boundary conditions are therefore given by Eqs. (A14) to (A17).

### 4. Analytical solution

The linear equations which must be solved are Eqs. (A14) to (A17) and (7). Each of these contain infinite sums which must be truncated in order to obtain a solution,

$$\sum_{p=-\infty}^{\infty} \to \sum_{p=-P}^{P}. \tag{A18}$$

This implies that the "B" unknowns are $B_p^{(m)}, 0 \leqslant m \leqslant M+1, -P < p < P$, so that there are $(M+2)(2P+1)$ unknowns for "B". The "A" unknowns are $A_p^{(m)}, 0 \leqslant m \leqslant M, -P < p < P$, so that there are $(M+1)(2P+1)$ unknowns for "A". The total number of unknowns is therefore $(2M+3)(2P+1)$. The number of equations in Eqs. (A14) and (A15) is $(M+1)(2P+1)$. The number of equations in Eqs. (A16) and (A17) is also $(M+1)(2P+1)$. The number of equations in Eqs. (7) is $2P+1$. Therefore, the total number of equations is $(2M+3)(2P+1)$ which is the same as the number of unknowns, so that the unknowns may be determined using standard methods for solving a system of simultaneous linear equations. The equations are

$$A_p^{(m)} e^{-ik_{yp}^{(m)} y^{(m)}} + B_p^{(m)} e^{ik_{yp}^{(m)} y^{(m)}} - A_p^{(m+1)} e^{-ik_{yp}^{(m+1)} y^{(m)}} - B_p^{(m+1)} e^{ik_{yp}^{(m+1)} y^{(m)}} = 0, \, 0 \leqslant m \leqslant M-1, \, -P \leqslant p \leqslant P, \tag{A19}$$

$$A_p^{(m)} e^{-ik_{yp}^{(m)} y^{(m)}} + B_p^{(m)} e^{ik_{yp}^{(m)} y^{(m)}} - B_p^{(m+1)} e^{ik_{yp}^{(m+1)} y^{(m)}} = \delta_{p0} H_0 e^{-ik_{y0}^{(m+1)} y^{(m)}}, \, m = M, \, -P \leqslant p \leqslant P, \tag{A20}$$

$$A_p^{(m)} C_p^{(m)} e^{-ik_{yp}^{(m)} y^{(m)}} - B_p^{(m)} C_p^{(m)} e^{ik_{yp}^{(m)} y^{(m)}} - A_p^{(m+1)} C_p^{(m+1)} e^{-ik_{yp}^{(m+1)} y^{(m)}} + B_p^{(m+1)} C_p^{(m+1)} e^{ik_{yp}^{(m+1)} y^{(m)}} = 0, \, 0 \leqslant m \leqslant M-1, \, -P \leqslant p \leqslant P, \tag{A21}$$

$$A_p^{(m)} C_p^{(m)} e^{-ik_{yp}^{(m)} y^{(m)}} - B_p^{(m)} C_p^{(m)} e^{ik_{yp}^{(m)} y^{(m)}} + B_p^{(m+1)} C_p^{(m+1)} e^{ik_{yp}^{(m+1)} y^{(m)}} = \delta_{p0} H_0 C_0^{(m+1)} e^{-ik_{y0}^{(m+1)} y^{(m)}}, \, m = M, \, -P \leqslant p \leqslant P, \tag{A22}$$

$$\sum_{q=-\infty}^{\infty} S_{qp} A_q^{(0)} - B_p^{(0)} = 0, \, -P \leqslant p \leqslant P. \tag{A23}$$

The unknowns of greatest interest are the $B_p^{(M+1)}$ because they are equivalent to the amplitudes $\rho_p$ of the Floquet-Bloch field components in Eq. (1) which govern the scattered field. For FB propagating components, instead

of $\rho_p$ it is preferable to employ the efficiency $\eta_p^\rho$ of coupling of power from the incident wave to the FB reflected wave $p$,

$$\eta_p^\rho = |\rho_p|^2 \cos\theta_p / \cos\theta_{\text{inc}}. \qquad (A24)$$

The angle $\theta_p$ between the direction of propagation of the $p$th FB wave and the $y$ axis is defined by Eq. (3). From Eqs. (1) to (2), a component of the FB series will be propagating (in contrast to being evanescent) if $k_{yp}^{(M+1)} = \sqrt{k^2 - k_{xp}^2}$ is real. For $\theta_{\text{inc}} = 0$ and $\theta_{\text{ref}} > 30°$, $k_{yp}^{(M+1)}$ is real for three values of $p$,

$$p = [-1, 0, 1], \theta_{\text{inc}} = 0, \theta_{\text{ref}} > 30°. \qquad (A25)$$

For the cases considered herein, $P = 2$. The computations required to compute the solutions of $A_p^{(m)}$, $B_p^{(m)}$, and subsequently the fields and the power coupling efficiencies, were performed by a Matlab program. This program requires a data file containing the S parameters $S_{qp}$, $-P \leqslant q \leqslant P$, $-P \leqslant p \leqslant P$.

## APPENDIX B: OPTIMIZATION SCHEME

As stated, it is assumed that the number $M$ of MMARC layers is given, and these layers arranged alternately from the bottom up with material with dielectric constant 10.2, dielectric constant 3, dielectric constant 10.2, etc. Therefore, the only degrees of freedom in the material are the layer thicknesses $h^{(m)}$. The coupling efficiencies in Eq. (A24) are therefore functions of these thicknesses,

$$\eta_p^\rho = \eta_p^\rho(h^{(m)}), 1 \leqslant m \leqslant M. \qquad (B1)$$

The goal of the optimization process is to solve the inverse problem: To determine the $h^{(m)}$ which produce desired values of $\eta_p^\rho$, where the possible values of $p$ are given in Eq. (A25). For the case of anomalous reflection, the target values of $\eta_p^\rho$ are

$$\eta_1^\rho = 1, \eta_{-1}^\rho = \eta_0^\rho = 0. \qquad (B2)$$

Since the sum of these efficiencies is unity, it is sufficient to find the $h^{(m)}$ which produce

$$\eta_1^\rho(h^{(m)}) = 1. \qquad (B3)$$

We employ a simple in-house algorithm for accomplishing this in two stages: a low-resolution stage followed by a high-resolution stage. These stages will now be considered separately. They will be applied to the two MMARC configurations of Fig. 4—one for which $M = 3$ [Fig. 4(a)], and the other for which $M = 5$ [Fig. 4(b)]—both MMARCs applied to the PCB-1 BPS shown in Fig. 3.

### 1. Low-resolution stage

A low-resolution sweep is performed to find the $\eta_1^\rho$ for all possible layer thickness combinations for which each $h^{(m)}$ is some integer multiple of an elementary thickness unit $\Delta_a$, where $0 \leqslant h^{(m)} \leqslant 0.5\lambda$. The configurations which produce $\eta_1^\rho$ closest to the target value 1 are used as starting values in the high-resolution stage. As an illustrative example of



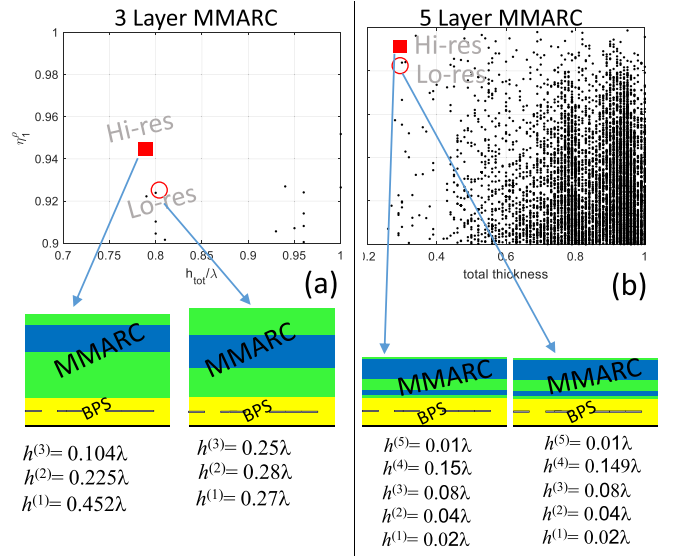FIG. 11. Anomalous reflection solutions for (a) $M = 3$-layer, and (b) $M = 5$-layer MMARC configurations, PCB-1 BPS of Fig. 3. For each $M$, "Lo-res" solutions are indicated as points in $\eta_1^\rho$-$h_{\text{tot}}$ space. For each $M$, the red-circled solution is chosen for "Hi-res" processing, leading to the final solution indicated by a red-filled-square. For each $M$, the MMARC configurations produced by the Lo-res solution and by the Hi-res solution are shown below the respective plot.

the low-resolution stage, consider $\Delta_a = 0.01\lambda$ applied to the MMARCs in Figs. 4(a) and 4(b). The thickness combinations which produce $\eta_1^\rho > 0.9$ are shown in Figs. 11(a) and 11(b) as black dots on an $\eta_1^\rho$ vs $h_{\text{tot}}$ graph, where $h_{\text{tot}} = \sum_{m=1}^{M} h^{(m)}$ is the total MMARC thickness. Each such dot represents an entire $M$-layer configuration for the MMARC. Comparing Figs. 11(a) and 11(b) clearly indicates that the two additional degrees of freedom provided by $M = 5$ not only increase the solution density, but also improve solution quality, providing $\eta_1^\rho$ values closer to unity for smaller overall thicknesses $h_{\text{tot}}$.

### 2. High-resolution stage

The highest quality Lo-res solution (circled in red in the figures) is used as the starting value in the Hi-res stage of the process, leading to the improved red-filled-square solution point that is also shown in the figures. In this Hi-res stage, a smaller resolution $\Delta_b \ll \Delta_a$ is used in order to converge on a layer configuration which will produce a value for $\eta_1^\rho$ larger than the one obtained in the low-resolution stage. Each iteration involves the following procedure, starting with layer $m = 1$. The thickness of $h^{(1)}$ is increased by $\Delta_b$. If the resulting $\eta_1^\rho$ increases, then $h^{(1)}$ is again increased by $\Delta_b$. This continues until there is no further increase in $\eta_1^\rho$. If there had been no increase in $\eta_1^\rho$ at all, then the $h^{(1)}$ is instead decreased by $\Delta_b$ until no increase in $\eta_1^\rho$ is discerned. After doing this for $h^{(1)}$, the same is done for $h^{(2)}$, and so forth until $h^{(M)}$ is completed. If during this entire iteration through all $M$ layers the $\eta_1^\rho$ has increased, then another iteration is performed. This is continued until there is no further increase in $\eta_1^\rho$.
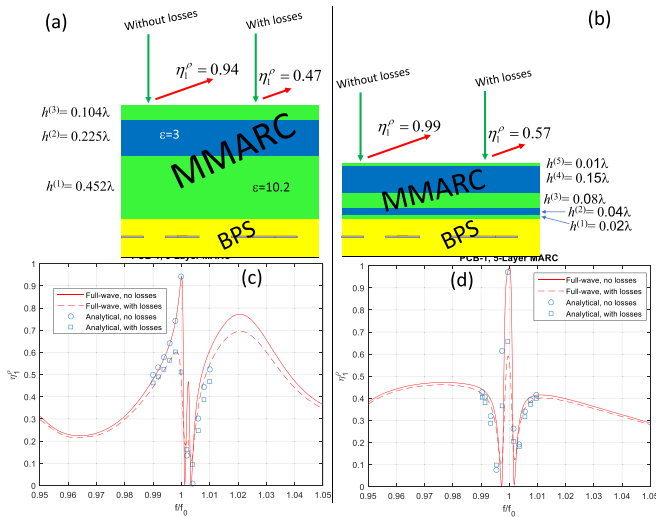
FIG. 12. $M = 3$-layer and $M = 5$-layer MMARC configurations for anomalous reflection, PCB-1 BPS of Fig. 3. [(a),(b)] The MMARC layer thicknesses which provide the CST-calculated coupling efficiencies, with and without losses, that are shown at the top of each figure. [(c),(d)] The CST-calculated and analytically-calculated $\eta_1^\rho$ frequency response, with and without losses, for the configurations in (a) and (b), respectively.

When this procedure is applied to the Lo-res results in Figs. 11(a) and 11(b) using $\Delta_b = 0.001$, the Hi-res solutions indicated by the red-filled square in each figure are obtained. In each of these figures, arrows from the Lo-res (red circle) and Hi-res (red-filled square) solutions in the plots point to the full MMARC configurations for these solutions. It may be seen that in obtaining the improved solution (from Lo-res to Hi-res) for $M = 3$, discernible changes have been made to the layer thicknesses; for $M = 5$, only a slight change in one of the layers was sufficient to improve the solution by one percent from $\eta_1^\rho = 0.98$ to $0.99$. This is likely due to the closeness of the Lo-res solution to unity in the case of $M = 5$.

## APPENDIX C: FREQUENCY RESPONSE AND DIELECTRIC LOSSES

In Figs. 4 and 5, results are presented which utilize the MMARC to produce anomalous effects for several types of BPS. For completeness, we provide here additional technical details related to these results with particular relevance to practical realization aspects. These would include the resultant devices' frequency responses with and without the presence of dielectric losses in the MMARC, as calculated using the analytical method and full-wave solvers. To establish the fundamental concepts and merit of the theoretical approach, the synthesis process was demonstrated using two dielectric materials in the MMARC, with permittivity corresponding to commercially available low-loss laminates offered by Rogers Corp., and dielectric loss was assumed negligible. Herein, to probe more accurately the potential for practical implementation, we consider the complete electromagnetic properties of these laminates, including the loss tangents provided by their specification data sheets: Rogers
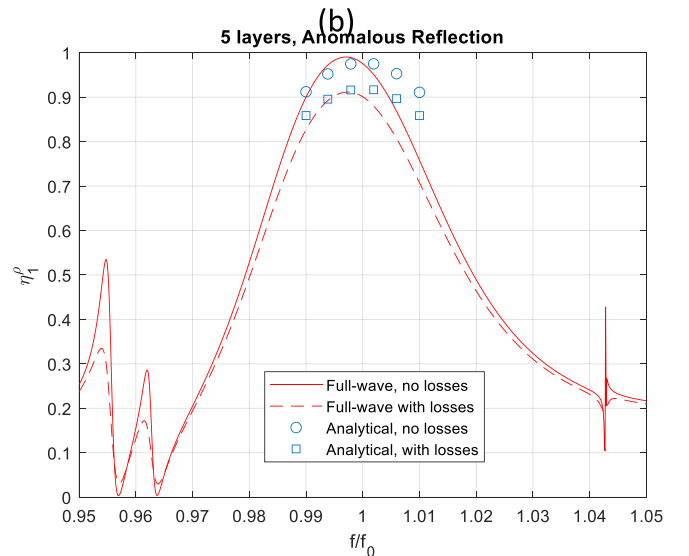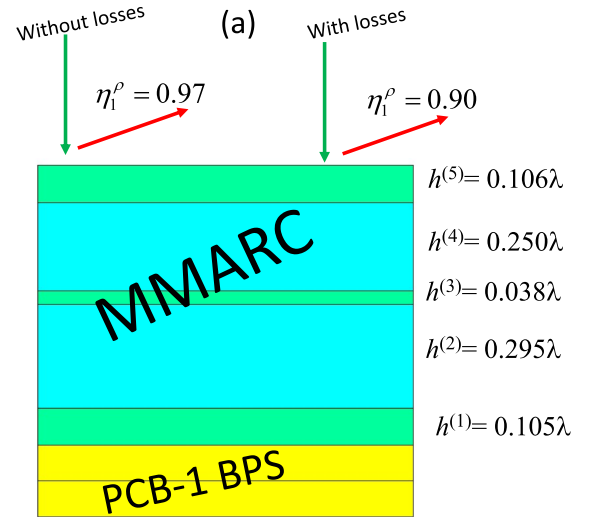


FIG. 13. (a) An analytically-optimized (OWL) configuration of a MMARC coating the PCB-1 BPS for anomalous reflection, producing the CST-calculated efficiencies shown near the top of the figure, with and without losses. The $\tan\delta$ losses in the MMARC were analytically accounted for in the optimization process. (b) Frequency response for configuration in (a).

RO3010 ($\epsilon_r = 10.2, \tan\delta = 0.0022$) and Rogers RO3003 ($\epsilon_r = 3, \tan\delta = 0.001$). The effects of these $\tan\delta$ losses will be analyzed for each of the standard anomalous reflection cases considered [corresponding to Figs. 4, 5(b), 5(d), 5(e), and 5(f)].

### 1. Optimization with losses (OWL)

As mentioned, in the applications in Figs. 4 and 5 and detailed below, the thicknesses of the MMARC layers were determined assuming negligible dielectric loss. Nonetheless, since our enhancement methodology relies on a robust analytical model as a basis for the optimization, the effect of losses can be readily incorporated into the formulation, thereby enabling resolution of an optimal MMARC *in the presence* of dielectric loss as well. This is accomplished
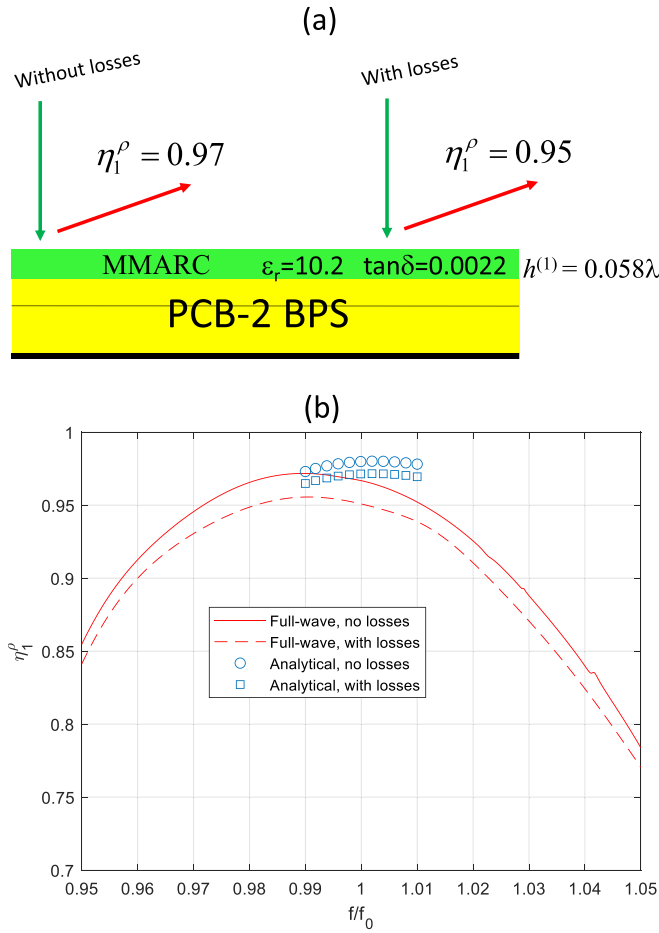
FIG. 14. Single-layer MMARC for anomalous reflection with PCB-2 BPS, corresponding to Fig. 5(b). (a) Physical configuration and reflection spectra with and without material losses. (b) CST and analytical calculations of frequency response, with and without losses, for configuration in (a).
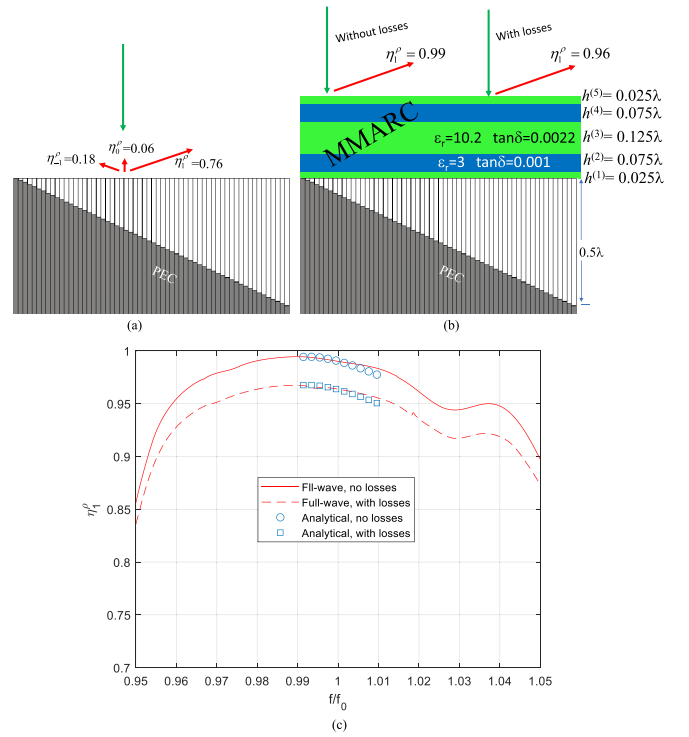


FIG. 15. Phase gradient metasurface-MMARC configuration for anomalous reflection. (a) The phase gradient metasurface without the MMARC, and the CST-calculated propagating components of the reflected Floquet-Bloch spectrum. (b) The phase gradient metasurface with the MMARC, and the CST-calculated propagating components of the reflected Floquet-Bloch spectrum, with and without $\tan\delta$ losses. (c) CST and analytical calculations of frequency response, with and without $\tan\delta$ losses, for configuration in (b).

directly in the analytical optimization process by replacing the real relative permittivity in Eq. (2) by the complex relative permittivity,

$$\varepsilon_r^{(m)} \to \varepsilon_r^{(m)}(1 + i\tan\delta^{(m)}), \tag{C1}$$

where $\tan\delta^{(m)}$ is the value of $\tan\delta$ in layer $m$ of the MMARC. The analytical optimization process in which realistic lossy dielectrics are employed will be referred to as "optimization with losses" (OWL), while the process in which lossless dielectrics are employed will be referred to as "optimization without losses" (OWOL). It will be shown that when these designs yield less-than-optimum anomalous reflection efficiencies, these efficiencies can be improved by re-designing the MMARC using OWL.

In Figs. 4 and 5(b), the BPS consists of one of two configurations of a printed circuit board (PCB). These are denoted PCB-1 and PCB-2 as shown in Fig. 3. They differ in the thickness of the upper layer and in the width of the middle metallic strip, as detailed in Fig. 3. In both cases, the BPS material corresponds to Rogers RO3003 substrate. Since the loss tangents of PCB-1 and PCB-2 were found to negligibly affect the scattering parameters of the bare BPS ($<0.02$ per

channel), the S matrices characterizing these BPSs are used herein as well.

### 2. Anomalous reflection, PCB-1 BPS

In Figs. 4(c) and 4(d), the CST-computed fields were compared with the analytically-computed fields for the PCB-1 BPS (see Fig. 3) coated by a three-layer and five-layer MMARC, respectively, for producing anomalous reflection. The layer thicknesses of the MMARCs in these cases are shown in Figs. 12(a) and 12(b). (These are the "Hi-res" solutions shown in Fig. 11.) Figures 12(c) and 12(d) display the respective frequency responses for the anomalously reflected mode, as calculated by a full-wave solver (CST), and by the analytical method. In Figs. 12(c) and 12(d), as well as in subsequent frequency response plots, the analytical results (circle-markers and square-markers) cover a much narrower region about the center frequency $f_0 = 20\,\text{GHz}$. The reason for this is that the analytical results are based on the S parameters that were found at the center frequency. When varying the frequency $f$, the analytical model still uses the same S parameters which were computed for frequency $f = f_0$, thereby introducing errors in results for other frequencies. It might be assumed that these S parameters would be acceptable in a region about the center frequency. Therefore analytical
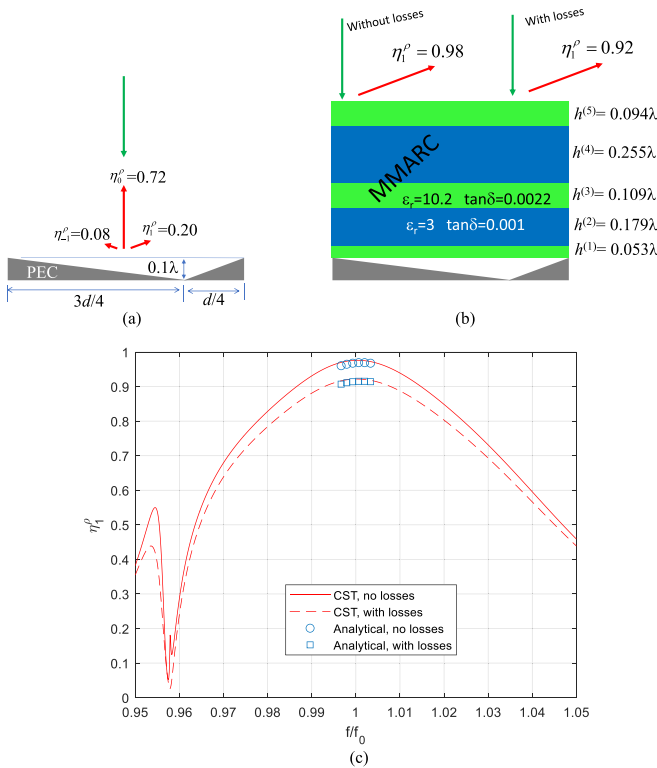
FIG. 16. (a) The sawtooth metasurface without the MMARC, and the CST-calculated coupling efficiencies. (b) The sawtooth metasurface with the MMARC, and the CST-calculated coupling efficiencies, with and without $\tan\delta$ losses. (c) CST and analytical calculations of frequency response, with and without losses, for configuration in (b).
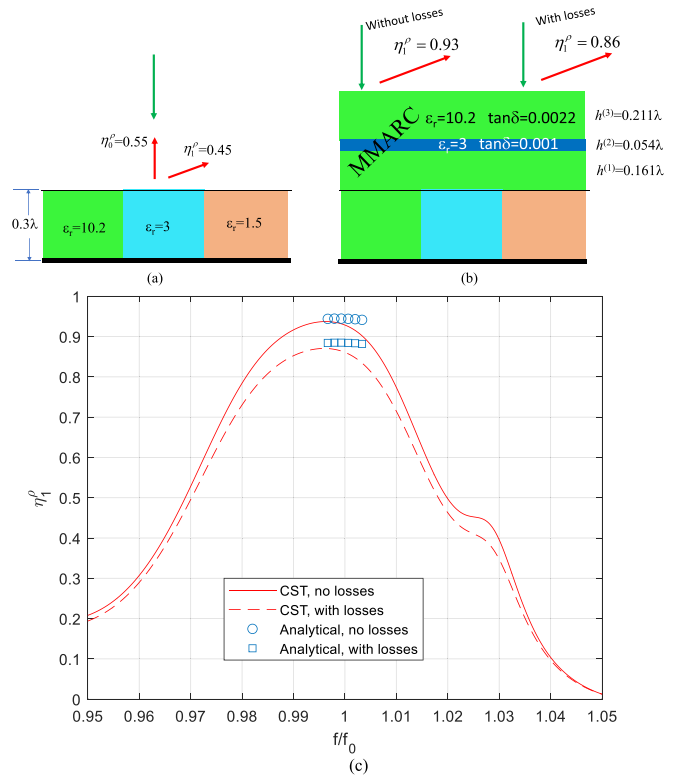


FIG. 17. (a) The tri-dielectric metasurface without the MMARC, and the CST-calculated propagating components of the reflected Floquet-Bloch spectrum. (b) The tri-dielectric metasurface with the MMARC, and the CST-calculated propagating components of the reflected Floquet-Bloch spectrum, with and without $\tan\delta$ losses. (c) CST and analytical calculations of frequency response, with and without losses, for configuration in (b).

results are given only for frequencies within 1% of the center frequency.

As can be seen in Figs. 12(a) and 12(b), the full-wave-calculated efficiencies *with losses* for both the three-layer and the five-layer MMARCs were over 0.40 below the efficiencies *without losses*. In Figs. 12(c) and 12(d), similar differences can be seen in the analytically-calculated efficiencies as well. This "unacceptable" result for lossy dielectrics was obtained using the MMARC thicknesses shown in Figs. 12(a) and 12(b) that were optimized for *lossless* dielectrics (OWOL, see Appendix C 1). However, as discussed in Appendix C 1, it is possible to use this analytically-formulated optimization model to determine MMARC thicknesses when the material *includes the losses* as the imaginary part of the relative permittivity [OWL, Eq. (C1)]. When OWL is employed, the completely different MMARC configuration of Fig. 13(a) can be obtained, and its frequency response is given in Fig. 13(b). Figure 13(b) includes CST-calculated and analytical results, with and without losses. Not only do the frequency responses in Fig. 13(b) have a wider band than those of Figs. 12(c) and 12(d), but the lossy-MMARC value of $\eta_1^\rho$ at the design frequency exceeds 0.9 in contrast to the less-than 0.6 shown in Figs. 12(c) and 12(d). As can be seen from the comparison between Figs. 12 and 13, the improvements in efficiency and bandwidth go hand in hand. Indeed, when no losses were present in the structure, a highly resonant

(high-Q) stack was chosen for the MMARC, leading, as one might expect, to narrowband performance and high sensitivity to losses. However, when losses are considered in the optimization process, a MMARC featuring a lower quality factor was found favorable and more resilient to losses, while at the same time exhibiting a wider operating frequency range.

Although, as mentioned, analytical frequency responses are given in Figs. 12 and 13 only for frequencies near the center frequency, this might be sufficient to estimate the expected bandwidth using the analytical model. (These figures clearly show that the analytical model can at least aid in estimating the second derivative of the anomalous reflection efficiency at/near the operating frequency.) In principle, then, it would be possible to encode bandwidth into the optimization process to obtain an optimal performance in regards to frequency response as well.

Clearly, then, the adverse effects of losses can be greatly alleviated by utilizing the OWL.

### 3. "Headstart" anomalous reflection, PCB-2 BPS

In Fig. 5(b), a single-layer MMARC was shown to produce anomalous reflection when coating the PCB-2 BPS. The precise dimensions, and the CST-calculated spectrum at the design frequency, with and without losses, are shown in
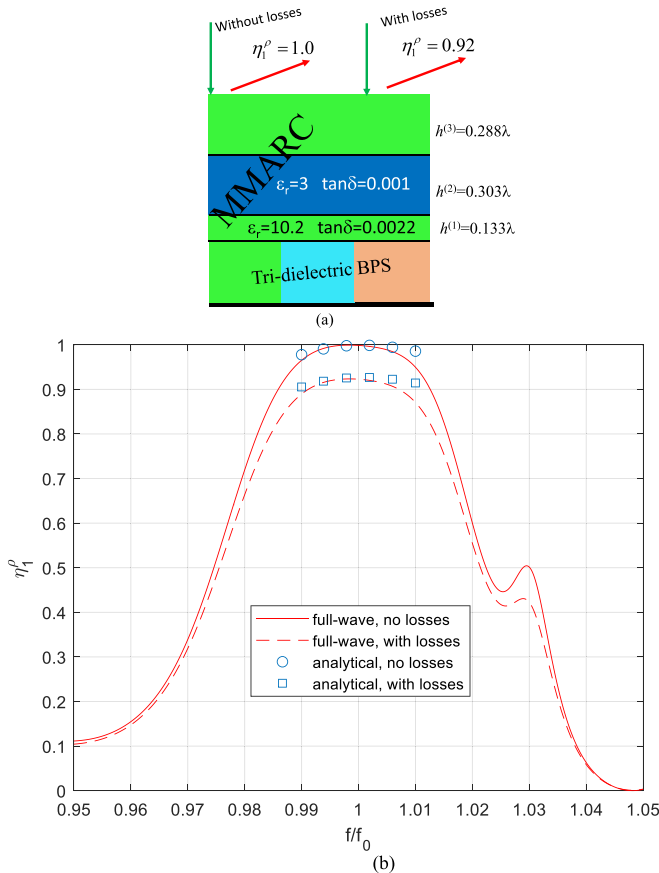
FIG. 18. An analytically-optimized (OWL) configuration of a lossy MMARC coating the tri-dielectric BPS of Fig. 17(a). The $\tan\delta$ losses in the MMARC were analytically considered in the OWL optimization process. These MMARC layer thicknesses provide the reflection coupling efficiencies that are shown near the top of the figure, with and without losses. (b) Frequency responses as calculated by CST and by the analytical method, with and without losses, for the configuration in (a).

Fig. 14(a). Even when losses are present, a high anomalous reflection efficiency of 0.95 is achieved. (The analytically computed spectrum is about 0.01 greater.) The CST-calculated and analytically-calculated frequency responses, with and without dielectric losses, are shown in Fig. 14(b). Even in the presence of dielectric losses, these frequency responses demonstrate strong anomalous reflection over a wide band, and reasonable agreement between the full-wave and analytical solutions. The fact that our MMARC in this case contains only a few reflective interfaces probably creates again a low-Q resonator. This, as mentioned previously, usually leads to larger bandwidths and reduced sensitivity to losses.

The reader is again reminded that in the analytical solution, the S parameters at the center frequency $f_0$ were employed, so that analytical frequency response results are provided only in the vicinity of $f = f_0$. Although these results in Fig. 14(b) display a slight frequency shift relative to the full-wave solution, these minor discrepancies may be related to the aforesaid inaccuracy in the S parameters.

### 4. Phase gradient anomalous reflection

In Fig. 5(d), a five-layer MMARC was shown to produce anomalous reflection when coating a phase gradient metasurface formed by parallel plate waveguides that are shorted at various distances. This is shown in Fig. 15. It is seen in Fig. 15(a) that without the MMARC, the efficiency in the anomalous direction is 0.76, while with the MMARC [Fig. 15(b)], this efficiency increases to 0.99 when the MMARC layers are assumed lossless, and to 0.96 when losses are present in the MMARC layers. The frequency responses of the anomalously reflected field component are shown in Fig. 15(c) as obtained from both the full-wave and analytical solutions. They demonstrate considerable bandwidth. The two solution methods provide essentially the same results near $f = f_0$. Again, the analytical results are given only near the frequency $f_0 = 20\,\mathrm{GHz}$, since the S parameters used to calculate these results [Eq. (7)] were obtained only for that frequency.

### 5. Sawtooth anomalous reflection

In Fig. 5(e), a five-layer MMARC was shown to produce anomalous reflection when coating a BPS that consists of a sawtooth-shaped conducting metasurface. The configurations, with and without the MMARC, are shown in Figs. 16(a) and 16(b). It is seen in Fig. 16(a) that without the MMARC, the efficiency in the anomalous reflection direction is 0.20, while with the MMARC [Fig. 16(b)], this efficiency increases to 0.98 when the MMARC is lossless, and to 0.92 when dielectric losses are present. The analytical model and CST computations differ by less than 1%. This may be seen from the frequency response shown in Fig. 16(c). This case study further demonstrates the ability of nonresonant MMARC structures–even in the presence of realistic loss–to provide dramatic increase of the efficiency, retained over a reasonable bandwidth.

### 6. Tri-dielectric anomalous reflection

In Fig. 5(f), a three-layer MMARC was shown to produce anomalous reflection when coating a tri-dielectric metasurface. This is shown in Fig. 17. It is seen in Fig. 17(a) that without the MMARC, the reflection coupling efficiency in the anomalous direction is 0.45. With the MMARC [Fig. 17(b)], this efficiency increases to 0.93 when the MMARC is lossless, and increases to only 0.86 when the MMARC layers are lossy. As may be seen in the frequency response plots in Fig. 17(c), the analytical model and full-wave results differ from each other by about 1% at the design frequency.

The relatively low coupling efficiency for anomalous reflection with a lossy MMARC (i.e., 0.86) is likely due to the fact that the OWOL optimization process was used (see Appendix C 1). Performing these optimizations with the OWL process instead produces the MMARC shown in Fig. 18(a). This lossy MMARC now produces a relatively high coupling efficiency of 0.92, while the coupling efficiency if the MMARC layers were lossless would startlingly be practically perfect. Both these values are appreciably higher than the corresponding efficiencies of the configuration in Fig. 17,

and the frequency band in Fig. 18(b) is wider than that in Fig. 17(c). The fact that the total thickness $0.73\lambda$ of the Fig. 18(a) MMARC is somewhat larger than the total thickness $0.43\lambda$ of the Fig. 17(b) MMARC is further sup-

porting evidence for relaxed resonant conditions in thicker layers. The larger phase accumulation facilitated by thick layers probably reduces the need for excessive multiple reflections.

---

[1] C. L. Holloway, E. F. Kuester, J. A. Gordon, J. O'Hara, J. Booth, and D. R. Smith, An overview of the theory and applications of metasurfaces: The two-dimensional equivalents of metamaterials, IEEE Antennas Propag. Mag. **54**, 10 (2012).

[2] S. A. Tretyakov, Metasurfaces for general transformations of electromagnetic fields, Philos. Trans. R. Soc. A **373**, 20140362 (2015).

[3] S. B. Glybovski, S. A. Tretyakov, P. A. Belova, Y. S. Kivshar, and C. R. Simovski, Metasurfaces: From microwaves to visible, Phys. Rep. **634**, 1 (2016).

[4] S. Sun, Q. He, S. Xiao, Q. Xu, X. Li, and L. Zhou, Gradient-index meta-surfaces as a bridge linking propagating waves and surface waves, Nat. Mater. **11**, 426 (2012).

[5] V. S. Asadchy, Y. Ra'di, J. Vehmas, and S. A. Tretyakov, Functional Metamirrors Using Bianisotropic Elements, Phys. Rev. Lett. **114**, 095503 (2015).

[6] P. Lalanne, S. Astilean, P. Chavel, E. Cambril, and H. Launois, Blazed binary subwavelength gratings with efficiencies larger than those of conventional échelette gratings, Opt. Lett. **23**, 1081 (1998).

[7] P. Lalanne, S. Astilean, P. Chavel, E. Cambril, and H. Launois, Design and fabrication of blazed binary diffractive elements with sampling periods smaller than the structural cutoff, J. Opt. Soc. Am. A **16**, 1143 (1999).

[8] E. Hasman, V. Kleiner, G. Biener, and A. Niv, Polarization dependent focusing lens by use of quantized Pancharatnam-Berry phase diffractive optics, Appl. Phys. Lett. **82**, 328 (2003).

[9] N. Yu, P. Genevet, M. A. Kats, F. Aieta, J.-P. Tetienne, F. Capasso, and Z. Gaburro, Light propagation with phase discontinuities: Generalized laws of reflection and refraction, Science **334**, 333 (2011).

[10] C. Pfeiffer and A. Grbic, Metamaterial Huygens' surfaces: Tailoring wave fronts with Reflectionless Sheets, Phys. Rev. Lett. **110**, 197401 (2013).

[11] F. Monticone, N. M. Estakhri, and A. Alù, Full Control of Nanoscale Optical Transmission with a Composite Metascreen, Phys. Rev. Lett. **110**, 203903 (2013).

[12] M. Selvanayagam and G. V. Eleftheriades, Discontinuous electromagnetic fields using orthogonal electric and magnetic currents for wavefront manipulation, Opt. Express **21**, 14409 (2013).

[13] A. Epstein and G. V. Eleftheriades, Synthesis of Passive Lossless Metasurfaces Using Auxiliary Fields for Reflectionless Beam Splitting and Perfect Reflection, Phys. Rev. Lett. **117**, 256103 (2016).

[14] A. Epstein and G. V. Eleftheriades, Passive lossless Huygens' metasurfaces for conversion of arbitrary source field to directive radiation, IEEE Trans. Antennas Propag. **62**, 5680 (2014).

[15] J. P. S. Wong, A. Epstein, and G. V. Eleftheriades, Reflectionless wide-angle refracting metasurfaces, IEEE Antennas Wirel. Propag. Lett. **15**, 1293 (2015).

[16] V. S. Asadchy, M. Albooyeh, S. N. Tcvetkova, A. Díaz-Rubio, Y. Ra'di, and S. A. Tretyakov, Perfect control of reflection and refraction using spatially dispersive metasurfaces, Phys. Rev. B **94**, 075142 (2016).

[17] A. Epstein and G. V. Eleftheriades, Arbitrary power-conserving field transformations with passive lossless omega-type bianisotropic metasurfaces, IEEE Trans. Antennas Propag. **64**, 3880 (2016).

[18] S. W. Marcus and A. Epstein, Fabry-Pérot Huygens' metasurfaces: On homogenization of electrically thick composites, Phys. Rev. B **100**, 115144 (2019).

[19] S. W. Marcus and A. Epstein, Electrically thick Fabry-Perot omega bianisotropic metasurfaces as virtual antireflective coatings and nonlocal field transformers, Phys. Rev. B **102**, 075144 (2020).

[20] S. W. Marcus and A. Epstein, Omega bianisotropic metasurfaces as Huygens' metasurfaces with anti-reflective coatings, *2020 Fourteenth International Congress on Artificial Materials for Novel Wave Phenomena (Metamaterials)*, 2020, pp. 361–363.

[21] H. K. Raut, V. A. Ganesh, A. S. Nairb, and S. Ramakrishna, Anti-reflective coatings: A critical, in-depth review, Energy & Environ. Sci. **4**, 3779 (2011).

[22] W. H. Southwell, Coating design using very thin high- and low-index layers, Appl. Opt. **24**, 457 (1985).

[23] D. Poitras and J. A. Dobrowolski, Toward perfect antireflection coatings. 2. Theory, Appl. Opt. **43**, 1286 (2004).

[24] D. J. Poxson, M. F. Schubert, F. W. Mont, E. F. Schubert, and J. K. Kim, Broadband omnidirectional antireflection coatings optimized by genetic algorithm, Opt. Lett. **34**, 728 (2009).

[25] Y. Ra'di and A. Alù, Metagratings for efficient wavefront manipulation, IEEE Photonics J. **14**, 1 (2022).

[26] Y. Ra'di, D. L. Sounas, and A. Alù, Metagratings: Beyond the Limits of Graded Metasurfaces for Wave Front Control, Phys. Rev. Lett. **119**, 067404 (2017).

[27] D. Sell, J. Yang, S. Doshay, R. Yang, and J. A. Fan, Large-angle, multifunctional metagratings based on freeform multimode geometries, Nano Lett. **17**, 3752 (2017).

[28] M. Memarian, X. Li, Y. Morimoto, and T. Itoh, Wide-band/angle blazed surfaces using multiple coupled blazing resonances, Sci. Rep. **7**, 42286 (2017).

[29] A. M. H. Wong and G. V. Eleftheriades, Perfect Anomalous Reflection with a Bipartite Huygens' Metasurface, Phys. Rev. X **8**, 011036 (2018).

[30] A. Epstein and O. Rabinovich, Unveiling the Properties of Metagratings Via a Detailed Analytical Model for Synthesis and Analysis, Phys. Rev. Appl. **8**, 054037 (2017).

[31] O. Rabinovich and A. Epstein, Analytical design of printed circuit board (pcb) metagratings for perfect anomalous reflection, IEEE Trans. Antennas Propag. **66**, 4086 (2018).

[32] V. Popov, F. Boust, and S. N. Burokur, Controlling Diffraction Patterns with Metagratings, Phys. Rev. Appl. **10**, 011002(R) (2018).

[33] C. Wan, R. Yang, Y. Shi, G. Zheng, and Z. Li, Visible-frequency meta-gratings for light steering, beam splitting and absorption tunable functionality, Opt. Express **27**, 37318 (2019).

[34] O. Rabinovich and A. Epstein, Arbitrary diffraction engineering with multilayered multielement metagratings, IEEE Trans. Antennas Propag. **68**, 1553 (2020).

[35] O. Rabinovich and A. Epstein, Dual-Polarized All-Metallic Metagratings for Perfect Anomalous Reflection, Phys. Rev. Appl. **14**, 064028 (2020).

[36] J. Yang, D. Sell, and J. Fan, Freeform metagratings based on complex light scattering dynamics for extreme, high efficiency beam steering, Ann. Phys. (Paris) **530**, 1700302 (2018).

[37] E. F. Kuester, M. A. Mohamed, M. Piket-May, and C. L. Holloway, Averaged transition conditions for electromagnetic fields at a metafilm, IEEE Trans. Antennas Propag. **51**, 2641 (2003).

[38] S. Tretyakov, *Analytical Modeling in Applied Electromagnetics* (Artech House, London, 2003).

[39] T. Tamir and S. Zhang, Modal transmission-line theory of multilayered grating structures, J. Lightwave Technol. **14**, 914 (1996).

[40] Https://www.3ds.com/products-services/simulia/products/cst-studio-suite/.

[41] Https://www.rogerscorp.com/-/media/project/rogerscorp/documents/advanced-connectivity-solutions/english/data-sheets/ro3000-laminate-data-sheet-ro3003—-ro3006—-ro3010—-ro3035.pdf.

[42] Y. Ra'di and A. Alù, Reconfigurable metagratings, ACS Photonics **5**, 1779 (2018).

[43] A. M. H. Wong, P. Christian, and G. V. Eleftheriades, Binary huygens' metasurfaces: Experimental demonstration of simple and efficient near-grazing retroreflectors for te and tm polarizations, IEEE Trans. Antennas Propag. **66**, 2892 (2018).

[44] D. H. Kwon, Lossless scalar metasurfaces for anomalous reflection based on efficient surface field optimization, IEEE Antennas Wirel. Propag. Lett. **17**, 1149 (2018).

[45] X. Wang, A. Díaz-Rubio, H. Li, S. A. Tretyakov, and A. Alù, Theory and Design of Multifunctional Space-Time Metasurfaces, Phys. Rev. Appl. **13**, 044040 (2020).

[46] Such protective coatings are not always required as seen in Figs. 5(d), 5(e), and 5(f) for non-PCB BPSs.

[47] In these figures, the incident wave has been analytically removed from the total fields in the uppermost region. Although the analytically-computed fields are available only above the BPS [$y > 0$, see Eq. (4)], the full-wave-computed fields include the BPS region.

[48] A. Díaz-Rubio, V. S. Asadchy, A. Elsakka, and S. A. Tretyakov, From the generalized reflection law to the realization of perfect anomalous reflectors, Sci. Adv. **3**, e1602714 (2017).

[49] A. Díaz-Rubio and S. A. Tretyakov, Acoustic metasurfaces for scattering-free anomalous reflection and refraction, Phys. Rev. B **96**, 125409 (2017).

[50] A. Díaz-Rubio and S. A. Tretyakov, Dual-Physics Metasurfaces for Simultaneous Manipulations of Acoustic and Electromagnetic Waves, Phys. Rev. Appl. **14**, 014076 (2020).

[51] N. Mohammadi Estakhri and A. Alù, Wave-Front Transformation with Gradient Metasurfaces, Phys. Rev. X **6**, 041008 (2016).

[52] S. W. Marcus and A. Epstein, Dynamic beam switching with shiftable multimodal anti-reflective coatings, in *2021 IEEE International Conference on Microwaves, Antennas, Communications and Electronic Systems (COMCAS)*, 2021, pp. 508–512.

[53] M. Mavridou and A. P. Feresidis, Dynamically reconfigurable high impedance and frequency selective metasurfaces using piezoelectric actuators, IEEE Trans. Antennas Propag. **12**, 5190 (2016).

[54] E. Abdo-Sánchez, A. Epstein, and G. V. Eleftheriades, Reconfigurability mechanisms with scanning rate control for omega-bianisotropic Huygens' metasurface leaky-wave antennas, IEEE Access **7**, 168247 (2019).

[55] E. Vassos, J. Churm, and A. P. Feresidis, Ultra-low-loss tunable piezoelectric-actuated metasurfaces achieving 360° or 180° dynamic phase shift at millimeter-waves, Sci. Rep. **10**, 15679 (2020).

[56] S. V. Hum and J. Perruisseau-Carrier, Reconfigurable reflectarrays and array lenses for dynamic antenna beam control: A review, IEEE Trans. Antennas Propag. **62**, 183 (2014).

[57] V. Popov, B. Ratni, S. N. Burokur, and F. Boust, Non-local reconfigurable sparse metasurface: efficient near-field and far-field wavefront manipulations, Adv. Optical Mater. **9**, 2001316 (2021).

[58] A. Pitilakis, O. Tsilipakos, F. Liu, K. M. Kossifos, A. C. Tasolamprou, D.-H. Kwon, M. S. Mirmoosa, D. Manessis, N. V. Kantartzis, C. Liaskos *et al.*, A multi-functional reconfigurable metasurface: Electromagnetic design accounting for fabrication aspects, IEEE Trans. Antennas Propag. **69**, 1440 (2021).

[59] Q. Xi, C. Ma, H. Li, B. Zhang, C. Li, and L. Ran, A reconfigurable planar Fresnel lens for millimeter-wave 5G frontends, IEEE Trans. Microwave Theory Techn. **68**, 4579 (2020).

[60] J. Coonrod, Understanding the variables of dielectric constant for PCB materials used at microwave frequencies, *2011 41st European Microwave Conference*, 2011, pp. 938–944.

[61] E. Abdo-Sanchez, M. Chen, A. Epstein, and G. V. Eleftheriades, A leaky-wave antenna with controlled radiation using a bianisotropic Huygens' metasurface, IEEE Trans. Antennas Propag. **67**, 108 (2019).

[62] O. Rabinovich, I. Kaplon, J. Reis, and A. Epstein, Experimental demonstration and in-depth investigation of analytically designed anomalous reflection metagratings, Phys. Rev. B **99**, 125101 (2019).